Enabling Efficient Uncertainty Quantification of Turbulent Combustion Simulations via Kinetic Dimension Reduction

by

Benjamin C. Koenig

S.B., Massachusetts Institute of Technology, 2021

Submitted to the Department of Mechanical Engineering
in partial fulfillment of the requirements for the degree of

Master of Science in Mechanical Engineering

at the

MASSACHUSETTS INSTITUTE OF TECHNOLOGY

June 2023

© Benjamin C. Koenig, 2023. All rights reserved.

Author . . . .
Benjamin C. Koenig
Department of Mechanical Engineering
May 12, 2023

Certified by. . . . .
Sili Deng
Assistant Professor of Mechanical Engineering
Thesis Supervisor

Accepted by . . . .
Nicolas Hadjiconstantinou
Professor of Mechanical Engineering
Graduate Officer

Enabling Efficient Uncertainty Quantification of Turbulent Combustion Simulations via Kinetic Dimension Reduction

by

Benjamin C. Koenig

Abstract

Propagating uncertainties in kinetic models through combustion simulations can provide important metrics on the reliability and accuracy of a model, but remains a challenging and numerically expensive problem especially for large kinetic mechanisms and expensive turbulent combustion simulations. Various surrogate model and dimension reduction techniques have previously been applied in order to reduce the cost of forward uncertainty propagation in combustion simulations, but these are often limited to low-dimensional, simple combustion cases with scalar solution targets. In the current work, a neural network-accelerated framework for identifying a low-dimensional active kinetic subspace was developed that applies to the entire temperature solution space of a flamelet table and can capture the mixture fraction and strain rate dependent effects of the kinetic uncertainty. The computational savings enabled by this novel framework were demonstrated through a proof-of-concept, flamelet-based application in a Reynolds-averaged Sandia Flame D simulation using a chemical mechanism for methane combustion with 217 reactions. By leveraging the large dimensional compression and low-cost scaling of the active subspace method, offloading the initial dimension reduction gradient sampling onto the laminar flamelet simulations, and accelerating the gradient sampling process with a specifically designed neural network, it was possible to estimate the temperature uncertainty profiles across the solution space of the turbulent flame with strong accuracy of $70 - 85\%$ using just seven perturbed solutions. Additionally, as it occurs entirely within the flamelet table, the cost of identifying the reduced subspace does not scale with the cost of the turbulent combustion model, which is a promising feature of this framework for future application to larger-scale and more complex turbulent combustion applications.

Thesis Supervisor: Sili Deng
Title: Assistant Professor of Mechanical Engineering

Acknowledgments

I would like to thank my advisor, Professor Sili Deng, for her guidance through the various challenges associated with this project and her continuous support through my career at MIT as an undergrad and graduate student. I'd like to thank Dr. Weiqi Ji as well for his knowledge and guidance, especially for his close mentoring and advice in the early stages of this project. I would also like to thank Professor Anthony Patera for years of academic mentoring, graduate school and career advice, and general support of my success at MIT; as well as Professor Pierre Lermusiaux for introducing me to the field of numerical fluid mechanics and computational engineering, and supporting my success throughout my research career.

I'd like to thank the machine learning subgroup of the Deng Energy and Nanotechnology group including Dr. Qiaofeng Li, Huaibo Chen, Stefan Borjan, and Edoardo Ramalli for their weekly discussion, advice, and support. I would also like to thank the rest of the DENG group over the past two years, including Maanasa Bhat, Suyong Kim, Valerie Muldoon, Gwendolyn Tsai, Dr. Yuesen Wang, Chuwei Zhang, and Dr. Jianan Zhang for supporting my ideas and creating a friendly work environment.

I would finally like to thank my family including my parents, Lisa and Phil, for their unconditional support of my academic career and constant pestering to remind me to put my best foot forward; and my brother Matt for his encouragement and friendship from 7,000 miles away.

Contents

List of Figures

List of Tables

Chapter 1

Introduction

1.1 Uncertainty in Turbulent Combustion Modelling

Turbulent combustion modelling is an important tool for design and optimization in many engineering fields. Traditional modelling approaches in gas turbines, internal combustion engines, and jet engines [1, 2, 3] can enable optimized designs with increased fuel efficiency and reduced emissions. Turbulent combustion is a major component in other processes as well, such as flame spray pyrolysis [4, 5] and lithium-ion battery thermal runaway [6, 7]. High-accuracy models in these applications can accelerate the development of advanced micro and nano-scale materials, and improve the thermal safety of increasingly prevalent lithium-ion batteries.

The multiscale and multiphysics complexities of the chemically reacting flow in turbulent combustion make it a difficult phenomenon to model accurately. Reynolds numbers in practical burners are often greater than 10^4 and in some cases exceed 10^6 [8], which itself presents a complex, multiscale, turbulent flow problem. Coupled to these flows are high-dimensional chemical kinetic mechanisms, detailed versions of which can contain hundreds to thousands of species and thousands to tens of thousands of reactions [9]. The two-way interaction of turbulent transport and strongly exothermic chemistry makes the coupling of these models expensive. Multimode phenomena are additionally present in many practical applications, from transient ignition to stable combustion and extinction [10]. Solid particle formation as soot or

material synthesis products [4, 11, 12] further complicates many models. A result of these coupled complexities is large computational expense for detailed simulations. State-of-the-art direct numerical simulation of turbulent combustion, for example, has costs in the millions of CPU hours [13, 14], even for domains on the sub-millimeter and sub-millisecond scales [15]. Large eddy simulations (LES) are cheaper thanks to the modelling approach for smaller turbulence scales, but still cost in the range of tens to hundreds of thousands of CPU hours for an entire combustor domain [12, 16, 17].

Another effect of the large number of coupled models and the model form simplifications that are needed to make these simulations tractable is a large amount of uncertainty. There are uncertainties tied to the various assumptions present in each of the component models of a simulation, such as those made when applying LES models to simplify turbulent flow [18, 19]. There are additionally uncertainties attached to the parameters used in each model. Turbulence model parameters [20, 21] and soot model parameters [21], even within a fixed model form, can have significant effects on simulation results. Kinetic model parameters are another key source of turbulent combustion simulation uncertainty, and are the focus of the remainder of this work.

The chemical model is an integral part of turbulent combustion simulations. Whether utilizing detailed or reduced chemistry, uncertain parameters in these models propagate forward through combustion simulations and can result in substantial uncertainties in the output profiles [16, 22, 23]. These output uncertainties and their sensitivities to model parameters are a key component in evaluating model results [24, 25, 26] and are often found to be large enough to account for nearly the entire discrepancy between the simulations and the experimental data [16, 27]. While quantifying the effects of kinetic uncertainties on the accuracy and precision of combustion simulations is important, such efforts are often expensive to carry out on a meaningful scale due to the high computational cost of turbulent combustion simulations as well as the previously discussed high dimensionality of detailed kinetic models [9].

1.2 Approaches for Efficient Uncertainty Quantification

Brute force Monte Carlo sampling is the most straightforward method for evaluating the effects of model parameter uncertainty on simulation results. With enough random samples within the uncertainty space of a high-dimensional kinetic model, statistics for the simulation results will converge to useful uncertainty ranges. Such sampling scales highly with the domain of the input uncertainty space, however, and is often too expensive to consider. To fully converge the statistics of a methane flamelet table, for example, which is the case investigated in this thesis, it was found in [16] that 50,000 samples had to be drawn and propagated forward. While possible in an inexpensive, laminar, one-dimensional flamelet, such propagation is infeasible or impossible for any multi-dimensional turbulent combustion simulation.

Many techniques have been proposed to alleviate the high cost of forward kinetic uncertainty propagation. In the remainder of this section, the current state of the art is discussed, and then a novel framework is proposed for forward kinetic uncertainty propagation that expands on these methods by considering a more general simulation target space, and by combining chemical reactions into vectors to provide further reduction in dimension and computational cost.

1.2.1 Surrogate Modelling and Sensitivity Analysis

A major challenge for uncertainty quantification in practical turbulent combustion simulations is the high computational cost associated with the simulations, which makes the forward problem expensive. Two main categories of methodology have been commonly applied in combustion research to alleviate the computational expense of repeated sampling. The first involves building low-cost surrogate models to replace the physical simulation. Polynomial chaos expansions (PCE) and high-dimensional model representations (HDMR), for example, are often used to leverage a relatively small number of expensive simulations in the construction of surrogate models, which

can be efficiently sampled in the forward uncertainty problem [27, 28]. However, these methodologies suffer from the "curse of dimensionality", making their construction inefficient in problems with a large kinetic mechanism [29, 30, 31]. A standard Hermite polynomial chaos expansion formulation [32], for example, may look like the following,

$$\theta(\mathbf{x}) \approx \sum_{k=0}^{P} \theta_k \Psi_k(\mathbf{x}), \quad \mathbf{x} = \{x_1, ...x_d\}, \tag{1.1}$$

where θ is the approximated function, $\mathbf{x}$ is the d-dimensional uncertain input, Ψ are the random polynomials fit to the simulation or experimental data using the coefficients θ_k, and P is the basis dimension. In this case, the number of polynomials scales as

$$P + 1 = \frac{(p+d)!}{p!d!}, \tag{1.2}$$

where p is the order of the polynomial chaos expansion. It is here that an exponential scaling of the number of terms in Eq. 1.1 with the input dimension d is observed [30], giving rise to the curse of dimensionality. Experiments performed to evaluate this dimensional scaling [32] have found a rapid deterioration of convergence rates in these expansions as the dimension d increases, and it was hypothesized that there exists some value d_{max} in the range of $d_{max} = 10 \sim 20$ above which sensitivity analysis is cheaper and more effective than response surface construction when using standard Monte Carlo methods.

Local sensitivity analyses and screening methods [33, 34, 35, 36] as well as newer artificial neural network-based surrogate methods [31, 37] are often used either to reduce the input space for the response surface algorithms or accelerate their computation. There exist many approaches to sensitivity analysis [38], with the end goal typically to identify which uncertain reactions have the greatest impact on simulation results. Many of these sensitivity analyses reveal that, especially in detailed kinetic mechanisms, a few uncertain reactions have outsized effects on simulation results. Responses surfaces can then be constructed using these reduced sets of key reactions, mitigating the problem of high dimensionality. Due to the substantial amount of

training data required from the physical solver, however, even with such accelerations these response surface-based methodologies are typically used only in cheaper, low-dimensional combustion cases such as ignition delay [27, 28], laminar flame speed [39, 40], or flow reactor [39] simulations, rather than complex flow fields.

The second general category of efficient uncertainty quantification involves methods that solve the forward problem directly in the physical solver, but leverage various techniques to reduce the total number of high-cost simulations needed. These are especially useful in expensive turbulent simulations where response surfaces cannot be feasibly constructed. The simplest approach might leverage the previously discussed local sensitivity analysis to deduce a reduced set of highly sensitive uncertain parameters for forward propagation with fewer samples required than the full set. The cost associated with this can still become large, however, since the identification of the reduced still suffers from the high dimensionality of the kinetic parameter space and the high cost of the turbulent simulation. Additionally, the reduced set itself may still contain on the order of ten or more sensitive reactions that must be sampled. In the following subsections, two newer techniques are detailed that allow for highly efficient forward uncertainty propagation in turbulent combustion simulations. These techniques leverage information from cheaper combustion problems and compress kinetic uncertainty further than standard sensivity analysis into low-dimensional vectors, providing a roadmap for accurate and efficient uncertainty quantification in certain turbulent combustion simulations with very few samples.

1.2.2   Flamelet Model Reduction

The first of these techniques involves identifying key assumptions in the turbulent combustion model being used for the full-scale, complex simulation, and then leveraging those assumptions to offload the computational expense of dimension reduction to a cheaper surrogate. Mueller et al. [16], for example, proposed a physics-informed dimension reduction based on the laminar flamelet concept [41]. This model takes advantage of the fact that, in the low Karlovitz number regime [42], or when the reaction zone of the flame is much smaller than the Kolmogorov turbulence length scale, there

is little interaction between the smallest scale of eddies and the flame sheet. This lack of interaction means that the turbulent flame can be modeled efficiently as an ensemble of laminar flamelets. The coupling between the non-equilibrium chemistry and turbulence can thus be simplified to the two parameters that define the flamelet's phase space: the mixture fraction and scalar dissipation rate. A flamelet look-up table can be precomputed based on cheap, one-dimensional laminar flamelets using the chemical kinetic model and turbulent simulation boundary conditions to provide the relationship between these two variables and the thermophysical state. Once constructed, the chemical kinetics used in the turbulent simulation are entirely contained within this mapping, and there is no further application of the high-dimensional kinetic model in the turbulent combustion simulation.

Mueller et al. [16] proposed that, as the chemical kinetics affect the turbulent simulation uniquely through the flamelet look-up table when using the flamelet model, instead of trying to fit surrogate models or perform sensitivity analysis on the target three-dimensional turbulent jet flame to reduce the 200+ dimensional kinetic uncertainty into something more tractable, it would be both cheaper and more meaningful to instead directly project the full kinetic uncertainty from the chemical model into the flamelet solution space for later propagation in the turbulent simulation. Doing so would reduce the high-dimensional uncertainty of the kinetic parameters into the low-dimensional space of flamelet solution variables such as temperature, species mass fractions, density, and viscosity. This reduction importantly does not involve any additional loss of information as is often the case with dimension-reducing techniques, as it leverages a simplification that is already assumed in the deterministic model. It additionally requires zero runs of the full-scale, three-dimensional turbulent jet flame, and is instead carried out fully within the orders of magnitude cheaper one-dimensional laminar flamelets. After reducing the kinetics, the authors of [16] narrowed the list of uncertain variables down to just three quantities that are necessary to evolve the LES equations: density, molecular viscosity, and molecular diffusivity. Then, to reduce the computational expense, they discarded the uncertainty in the latter two and investigated the uncertainty in the density only, allowing them to

use just seven samples of a single uncertain parameter in the full-scale simulation to quantify its uncertainty.

Leveraging the projection that was already present in the computational model led to a powerful estimate of the effect of kinetic uncertainty on the expensive turbulent simulation investigated in [16] with just seven samples (compared to the hundreds of reactions in the full kinetic parameter space). It also highlighted a need for such physics-informed uncertainty quantification methods in expensive turbulent combustion simulations. The investigated flame was reported to take 10,000 cpu hours per simulation, making surrogate modelling or sensivitity analysis efforts infeasible, even for a reduced mechanism. However, the application of the flamelet-based reduction here left open certain questions about the accuracy and kinetic interpretability of such a reduction. The elimination of uncertainty in the molecular viscosity and molecular diffusivity was reasonable given the computational expense of the simulation being investigated, but also leads to the possibility that certain uncertain physics were not accurately represented in the density-only results. Additionally, the abstraction of kinetic perturbations and density perturbations using the flamelet model leads to uncertainty results that, while informative, cannot be traced back or analyzed in terms of the uncertain reactions themselves, limiting the scope of application. Similar works investigating physics-informed dimension reduction regimes similar to the flamelet model have followed, such as applying ignition delay time kinetic reductions for the prediction of liftoff height in turbulent flames [22, 43]. The next section involves discussion of a tool that allows for dimensional compression in the original input kinetic space down to spaces of similarly low dimension as those investigated in [16], which could enable such physics-informed dimension reduction while also providing kinetic interpretability and reasonable error estimates.

1.2.3   Active Subspaces

The active subspace method [22, 29, 44] is another approach for identifying reduced kinetic spaces for efficient sampling. Unlike traditional kinetic sensitivity methods that identify an active subset of important reactions, this algorithm identifies active

linear combinations of important reactions (active subspaces) that most impact the quantity of interest. This is similar conceptually to principal component analysis, though it identifies directions in the gradient space and thus in the input kinetic parameters rather than the output state vectors [45], and performs such a reduction globally across the entire uncertainty space rather than locally at the nominal values [46]. The coupled information contained in each of these subspace directions allows for greater reduction than typical sensitivity analyses or response surface-based methods, often down to even a single subspace direction [22, 29, 43, 21], and thus greater computational savings in the forward propagation step. If ten reactions are all highly sensitive, for example, then traditional sensitivity-based methods would call for a ten-dimensional sampling and forward propagation. In the referenced works, however, it was often found that even with multiple dominant reactions, the active subspace method is able to find linear combinations of the key reactions that compress the output response to their uncertainties into just one direction within the high-dimensional uncertainty space, leading to a more efficient one-dimensional sampling and forward propagation. The active subspace method is particularly useful in problems with high input dimension, as is often the case with chemical kinetic uncertainty, since it partially avoids the curse of dimensionality thanks to its relatively low dependence on input dimension size [47, 48]. This is especially true for problems with low-dimensional active subspaces, which have an even smaller cost dependence on problem size.

Previous combustion applications of the active subspace algorithm have typically investigated only a single quantity of interest at a time such as liftoff height [22, 43], ignition delay time [22, 43, 49], combustor exit pressure [50], or scalar soot metrics [21]. These results all indicated the powerful dimension reduction capability of the algorithm through their often one-dimensional final subspaces, but were limited by the original active subspace formulation to investigating these single quantities only. Ji et al. [29] expanded on this concept by investigating shared low-dimensional subspaces that were capable of representing the kinetic uncertainty across multiple target quantities. There, active subspaces were computed for each scalar output quantity,

and then in a second processing step these scalar subspaces were combined to create shared subspaces that could represent the physics of various simple combustion phenomena, such as ignition delay time and laminar flame speed, for a range of fuels. Various active subspace works have also leveraged and validated physics-informed simplifications of kinetic uncertainty, similar to the flamelet approach discussed in Section 1.2.2, in various configurations, such as ignition delay time as a predictor of liftoff height [22, 43]. Such applications benefit in two substantial ways from this combination of physics-informed active subspace reduction. By leveraging the theoretical connection between ignition delay time and turbulent flame liftoff height, the authors were able to sample repeatedly in the much cheaper ignition delay time simulations to constuct their reduced uncertainty spaces, before applying them efficiently in the turbulent flames. Additionally, by choosing the active subspace algorithm for the identification of these reduced uncertainty spaces, the authors in both cases were able to find a single active subspace direction along which to efficiently sample in the turbulent flame, minimizing the cost needed to quantify the uncertainty in these cases. The liftoff height quantity of interest in the turbulent flame notably remains a scalar quantity, however, and it can be presumed that such a subspace derived using ignition delay results only is not applicable to other targets within the turbulent simulation profile. The combination of multi-target active subspaces and a physics-informed kinetic uncertainty simplification was proposed in Koenig et al. [51], where a low-dimensional subspace was found to accurately represent the kinetic uncertainty across the entire temperature profile of a laminar flamelet. An interesting result here was that while one-dimensional subspaces were prevalent at each individual mixture fraction location in the flamelet, the combined uncertainty response of the entire flamelet required at least two subspace directions to capture with high accuracy. This result was similar to that of [29], where shared subspaces of low yet greater than one dimension were found when combining various one-dimensional subspaces at different conditions. While meaningful, the result of [51] was limited to a single flamelet and did not investigate the full flamelet table required to apply the subspace to a turbulent simulation, inspiring further work in this area of multi-target, physics-informed

kinetic subspace identification.

1.3 Research Objectives

In this work, a complete forward kinetic uncertainty propagation framework for turbulent combustion in the flamelet regime is proposed and demonstrated, starting from an uncertain mechanism and ending with turbulent simulation uncertainty profiles. An artificial neural network surrogate model is created to accelerate the active subspace reduction process, which was performed here on the full two-dimensional phase space of a flamelet table. The inexpensive gradients sampled from this neural network were used to reduce the high-dimensional kinetic uncertainty of the entire flamelet table into a low-dimensional active subspace. The effects of kinetic uncertainty on the simulation of Sandia Flame D were then quantified, and comparisons were drawn between output uncertainty profiles obtained via efficient sampling in the active subspace and via brute force Monte Carlo sampling in the full kinetic space. This framework operates efficiently on both ends of the problem at hand - it identifies a remarkably low dimension kinetic uncertainty space that applies across a much broader input space than what is typically investigated in combustion uncertainty research. This scale of reduction, demonstrated through the two-dimensional, Reynolds-averaged turbulent combustion simulation shown here, has the potential to be scaled up to facilitate forward uncertainty propagation in more expensive cases, such as large eddy simulations in the flamelet regime.

Chapter 2

Methods

This work expands on the kinetic subspace investigation method proposed in [51] and applies it to the full temperature solution space of a nonpremixed flamelet table. The kinetic uncertainty across the entire two-dimensional input of a flamelet table is reduced in an artificial neural network-powered, two-stage subspace identification process to a single global active subspace. By virtue of the steady laminar flamelet model, this active subspace is in theory directly applicable to a larger-scale turbulent combustion simulation. Its performance is this context is evaluated in the forward kinetic uncertainty propagation of a nonpremixed turbulent flame simulation. An overview of this entire framework, which leverages the kinetic similarity among the flamelets representing the thermochemical states of the turbulent flame, is presented in Fig. 2-1 along with a general comparison of its key advantages compared to standard sensitivity-based forward propagation. The following subsections describe each step in detail.

2.1 Kinetic Subspace Discovery

The framework begins with the active subspace algorithm, specific details of which motivate construction of a neural network surrogate model (described later in this section). The generic algorithm, methodology, proofs, and kinetic discussion for the active subspace method are presented in [44] and [51]. Below are a handful of key
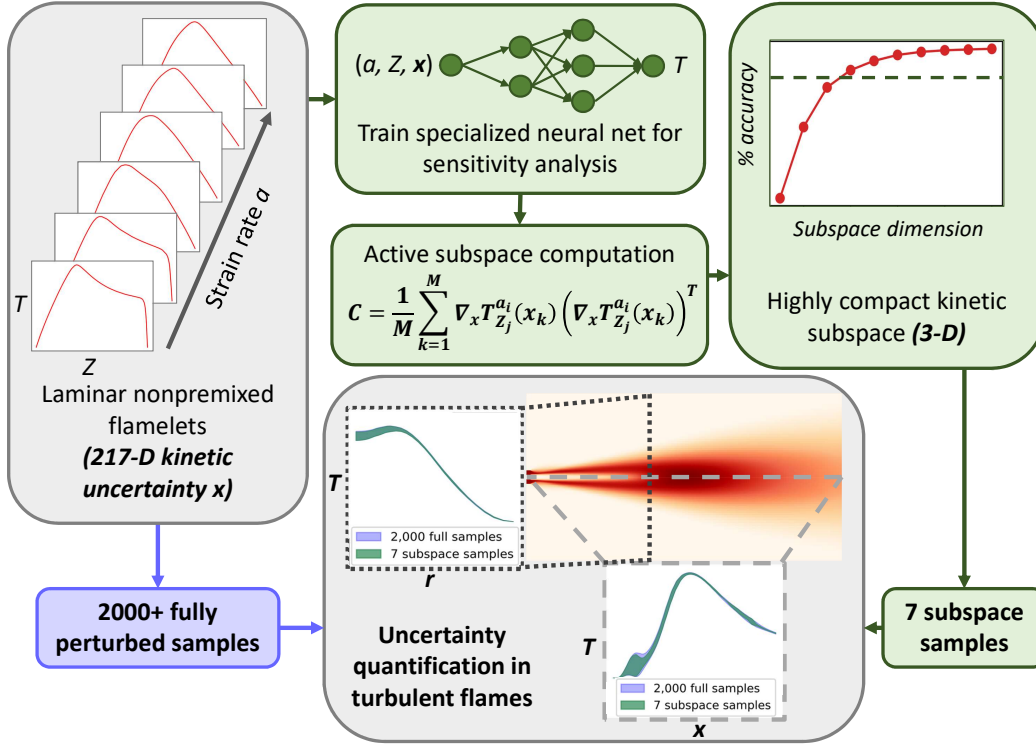
Figure 2-1: Overview of the methodology used to efficiently propagate kinetic uncertainty in this work. The 217-dimensional kinetic uncertainty is reduced across the entire flamelet table to a three-dimensional active subspace within which efficient sampling for forward propagation is performed. Accuracy benchmarking is then done against a much larger sample (2,000 samples) of fully perturbed mechanisms. Highlighted here are key advantages of the proposed framework including large dimensional compression and kinetic reductions that are applicable to the entire turbulent flame profile.

variable definitions, after which an overview of the active subspace algorithm, adapted from [44], is presented.

All flamelet data used for subspace discovery was generated in Cantera [52] using a tailored form of the GRI-Mech 3.0 mechanism [53] with 217 reactions neglecting NOx chemistry. All uncertain kinetic parameters are perturbed within the ranges given in the literature [54],

$$x_\ell = \frac{\ln k_\ell/k_{\ell,0}}{\frac{1}{3}\ln u_\ell} \sim \ N(0,1), \tag{2.1}$$

where x_ℓ is the ℓth index of the normalized rate constant perturbation vector $\mathbf{x}$, k_ℓ is the perturbed value of the ℓth rate constant, $k_{\ell,0}$ is the nominal value of the ℓth rate constant, u_ℓ is the uncertainty factor corresponding to $k_{\ell,0}$ as reported in [54], and $N(0,1)$ denotes the standard normal distribution with zero mean and unit variance. The following mean strain rate formulation was used throughout discussion of the flamelets for consistency,

$$a = (Q_{fuel} + Q_{oxidizer})/2D, \tag{2.2}$$

where Q is the volumetric flow rate on either the fuel or oxidizer side, and D is the width of the counterflow domain. Finally, the hydrogen mixture fraction Z is defined identically to [51] as

$$Z = \frac{W_{\mathrm{mix}} - W_{\mathrm{ox}}}{W_{\mathrm{fuel}} - W_{\mathrm{ox}}}, \tag{2.3}$$

where Z is the mixture fraction at a given location, and W_{mix}, W_{ox}, and W_{fuel} represent the hydrogen mass fractions of the mixture, oxidizer stream, and fuel stream, respectively.

The aim of the kinetic subspace discovery process is to identify an r_u-dimensional subspace in the d-dimensional kinetic rate constant space (with $r_u << d$) that describes the bulk of the temperature variation across an arbitrarily strained flamelet, at any given mixture fraction. That is, at any strain rate a and mixture fraction Z, the goal of the subspace is to accurately approximate the temperature response T_Z^a to any kinetic perturbation,

$$T_Z^a(\mathbf{x}_d) \approx T_Z^a(\mathbf{x}_{r_u}), \tag{2.4}$$

where $\mathbf{x}_d$ is a full-rank vector of rate constant perturbations for the d reactions in the kinetic model, while $\mathbf{x}_{r_u}$ is the same vector expressed with only the r_u basis directions

present in the subspace. Such a reduction allows for forward sampling in just r_u dimensions, which given $r_u << d$ indicates large savings for forward uncertainty propagation.

2.1.1 Reduction at a Single Location in the Flamelet Table

In order to identify the subspace that applies globally in Eq. 2.4, the first step is a traditional single-target subspace. For a fixed strain rate a_i and a fixed mixture fraction Z_j, the quantity of interest is the scalar flamelet temperature $T_{Z_j}^{a_i}(\mathbf{x})$, which for Eqs. 2.6 and 2.7 is denoted as

$$T \equiv T_{Z_j}^{a_i}(\mathbf{x}). \tag{2.5}$$

The matrix $\mathbf{C}$ is defined as the expected value of the outer product of the gradient of this temperature evaluation with respect to the kinetic parameters across the uncertainty range defined in Eq. 2.1, and its eigendecomposition is evaluated as

$$\mathbf{C} = \mathbb{E}[(\nabla_{\mathbf{x}}T)(\nabla_{\mathbf{x}}T)'] = \mathbf{W}\Lambda\mathbf{W}'. \tag{2.6}$$

Here Λ and $\mathbf{W}$ contain the eigenvalues λ_i and eigenvectors $\mathbf{w}_i$ of C, respectively, in order of largest to smallest eigenvalue. Through manipulation of Eq. 2.6, the identity $\lambda_i = \mathbf{w}_i'\mathbf{C}\mathbf{w}_i$ for any index i, and the symmetry of the gradient outer product, it can be shown that

$$\lambda_i = \mathbf{w}_i'\mathbf{C}\mathbf{w}_i = \mathbf{w}_i'(\mathbb{E}[(\nabla_{\mathbf{x}}T)(\nabla_{\mathbf{x}}T)'])\mathbf{w}_i = \mathbb{E}[((\nabla_{\mathbf{x}}T)'\mathbf{w}_i)^2]. \tag{2.7}$$

This result shows that the mean squared directional derivative of the temperature T with respect to a given eigenvector $\mathbf{w}_i$ equals the eigenvalue λ_i. In other words, across the uncertainty space defined by $\mathbf{x}$, it is expected that the directions in the kinetic space described by the eigenvectors corresponding to the highest eigenvalues carry the largest directional derivatives and thus have the largest impact on the uncertainty of the temperature T. On the other hand, this result also indicates that T does not

respond significantly to kinetic perturbations that align with the eigenvectors corresponding to near-zero or relatively small eigenvalues. It can additionally be asserted based on the symmetry of the gradient outer product that the eigendecomposition forms an orthogonal basis of eigenvectors, or a rotation of the original d-dimensional basis vectors. By selecting the eigenvectors corresponding to the largest eigenvalues only, this basis can be truncated to include only the most information-dense directions in the kinetic parameter space for forward uncertainty propagation. This reduced set of directions is labeled the active subspace. Deeper analysis of this algorithm is available in [44].

In practice, the expected value of Eq. 2.6 can be approximated by sampling repeatedly throughout the kinetic uncertainty space, as per

$$\mathbf{C} \approx \frac{1}{M} \sum_{k=1}^{M} \nabla_x T_{Z_j}^{a_i}(\mathbf{x}_k)(\nabla_x T_{Z_j}^{a_i}(\mathbf{x}_k))^T = \mathbf{W} \Lambda \mathbf{W}^T. \tag{2.8}$$

Here, M is the total number of rate constant samples k that are generated from the full uncertainty space in $\mathbf{x}$, with the gradient $\nabla_x T_{Z_j}^{a_i}(\mathbf{x}_k)$ evaluated once per iteration k. As per the analysis of Eq. 2.7, the eigenvalues of this decomposition at a given (a_i, Z_j) pairing represent the mean squared directional derivatives of the temperature with respect to each eigenvector, providing a measure of relative importance. By selecting the first index m where $\lambda_m >> \lambda_{m+1}$ and recalling that the eigenvalue list is ordered by magnitude, a reduced subspace of dimension m can be found that captures the bulk of the variance in the temperature gradients $\nabla_x T_{Z_j}^{a_i}$ across the uncertainty range. In the remainder of this work, it is assumed that $m = 1$, based on the result of [51] and on heuristics presented later in Section 3.2.2. $\mathbf{w}_{1,(i,j)}^{local}$, the first eigenvector truncated from $\mathbf{W}$, is therefore defined as the one-dimensional subspace that applies to the point (a_i, Z_j) in the flamelet table. By virtue of the M samples in Eq. 2.8 across the entire uncertainty space, this single-target subspace is itself a global sensitivity measure. The superscript "local" here is used to emphasize that this subspace was discovered at (and is applicable to) a single (a_i, Z_j) location in the flamelet table.

Carrying out the reduction of Eq. 2.8 from the full kinetic uncertainty space down

to a single eigenvector direction at some flamelet table location (a_i, Z_j) provides a one-dimensional subspace that captures, with strong accuracy, the global uncertainty at that point in the flamelet table. However, it is not a given that this one-dimensional subspace applies at other locations in the flamelet table as well. In fact, it was found in [51] that even at a fixed strain rate, the dominant kinetic subspace direction (as well as the set of highly sensitive reactions) changed substantially enough across the mixture fraction domain of the flamelet such that any one (a_i, Z_j)-specific subspace would fail to sufficiently represent the temperature response at other locations in the flamelet. In that case, a second stage of reduction was proposed across the mixture fraction space of the target flamelet, which searched for similarity across these single-target subspaces and led to a high accuracy, low-dimensional subspace that was applicable to the full mixture fraction domain of the target flamelet. The current work investigates the scaling up of such a reduction from a single scalar target to not just to an entire flamelet, but an entire flamelet table including flamelets at strain rates in a wide range of four orders of magnitude. The second stage of reduction, which begins with the set of $(n_i \cdot n_j)$ one-dimensional, single-target subspaces at each each location (a_i, Z_j) in the flamelet table, is detailed in the following subsection.

2.1.2 Reduction Across the Entire Flamelet Table

After performing the single-target reduction of Eq. 2.8 at each location (a_i, Z_j) in the flamelet table, the matrix $\mathbf{A}$ is constructed as the $(n_i \cdot n_j) \times d$ matrix of all 1-D local subspaces $\mathbf{w}_{1,(i,j)}^{local}$, where n_i and n_j are the total number of strain rate and mixture fraction locations, respectively, and each row of $\mathbf{A}$ is the corresponding $1 \times d$ local subspace vector from Eq. 2.8. $\mathbf{A}$ therefore has a very large aspect ratio, where each column represents a specific chemical reaction and each row is that reaction's contribution to a single local subspace. Depending on the results of Eq. 2.8 it is also possible to use multi-dimensional local subspaces in the construction of $\mathbf{A}$, though in this work only one-dimensional local subspaces are considered based on the highly one-dimensional results of [51] as well as discussion in Section 3.2.2 of the performance of such an assumption. It is rather obvious based on the aspect ratio of

A (or identically from the fact that $(n_i \cdot n_j) > d$) that some degree of correlation exists across the $(n_i \cdot n_j)$ local subspace vectors. It can be further expected, however, that this correlation is large due to the nature of the similar outputs being investigated, and that a second stage of reduction will be capable of discovering a more general, low-dimensional subspace that applies to the entire flamelet table. As in [51], though here with n_i times more rows, the singular value decomposition (SVD) of **A** is taken as,

$$\mathbf{A} = \mathbf{U}\mathbf{S}\mathbf{V}^T, \tag{2.9}$$

where **S** is an $(n_i \cdot n_j) \times d$ diagonal matrix with d singular values σ that correspond to the relative importance of the principal directions contained in **V**. This is analogous to a second application of the principal component analysis of Eq. 2.8, though the covariance matrix is now defined using the local subspaces instead of the temperature gradients. Additionally, while Eq. 2.8 reduced at fixed flamelet locations across the full uncertainty space to a series of local subspaces, Eq. 2.9 now reduces that set of local subspaces across the entire flamelet phase space to a final universal subspace. Based on this mathematical similarity, the interpretation of the singular value decomposition of **A** is similar to the eigendecomposition of **C**. The squared singular values σ^2 relate to the eigenvalues of the matrix $\mathbf{A}\mathbf{A}^T$, and are used to decide r_u, the dimension of the final subspace. In this case, a clear dropoff in magnitude did not exist in the low-r_u space, so instead the selection is based on the percentage of variance captured by a given r_u, that is, how much of the total sum of all σ^2 is represented by the sum of those σ^2 from indices 1 to r_u. After selecting r_u, a reduced space $\mathbf{w}_m$ is extracted from **V** with m ranging from 1 to r_u. The key generalization of this work is in the $(n_i \cdot n_j)$ sized **A** matrix that includes both the mixture fraction and strain rate input spaces of the flamelets. Thus, the final r_u-dimensional subspace discovered here describes the kinetic uncertainty of the entire two-dimensional input space of a flamelet table, in contrast to the one-dimensional mixture fraction space investigated in [51] (or the zero-dimensional quantities of interest typically examined

with the generic active subspace method).

2.2   Surrogate Model Neural Network

The active subspace method partially avoids the curse of dimensionality thanks to its low dependence on input dimension size [29]. The use of one-dimensional local subspaces further decreases the subspace generation cost in Eq. 2.8 [47, 48]. However, due to the two-dimensional flamelet input space investigated, $\sim 10^4$ local subspaces are required to construct $\mathbf{A}$ in Eq. 2.9. The absolute lowest possible number of gradient evaluations per local subspace is 22 as per the generic dimensional scaling proposed in [48]. A more reasonable number based on the same scaling laws with mid-range parameters is 100, while the scaling rules typically used in combustion applications [22, 21] would call for over 1,000 based on the large dimensionality of the kinetic problem investigated here. The expected grand total of gradient evaluations is therefore on the order of $10^6 \sim 10^7$.

2.2.1   Neural Network Architecture

To reduce the computational cost associated with gradient computation, a neural network surrogate model was developed with a physics-based structure inspired by Nonlinear Independent Dual Systems [55] and Deep Operator Networks (DeepONet) [56]. Artificial neural networks have been found to be more efficient than PCE and HDMR response surfaces for a kinetic uncertainty problem of similarly large dimension as the methane mechanism investigated here [57], and are also well-suited to efficient gradient evaluation by virtue of the backpropagation algorithm [58], as argued and demonstrated in [51]. DeepONet-type networks have also seen use in various recent combustion applications [51, 59, 60]. The network structure used here, shown in Fig. 2-2, is similar to that used in [51]. Key features include grid independence, where the inclusion of mixture fraction and strain rate as input nodes allows for training on data with arbitrarily refined grids and then downstream application on a single grid for consistency; and inductive bias, where the splitting of the two fundamentally dif-

ferent inputs (kinetics and boundary conditions vs. flame sampling location) encodes existing physical knowledge of the problem's structure into the network, potentially easing the burden of learning the remaining physics and thus the cost of training. Here grid independence is the major advantage of this specific network structure, as it allows for the use of Cantera training data solved on actively refined grids (which vary throughout the kinetic uncertainty space) without interpolation. Similarly, they allow for user-specified grids for subspace sampling in the downstream step, further enabling flexibility and efficiency without the need for error-prone interpolation. The key difference here when compared to the network of [51] is the strain rate parameter input node, which allows the network to learn (and compute gradients for) the entire flamelet table, rather than just a single flamelet.
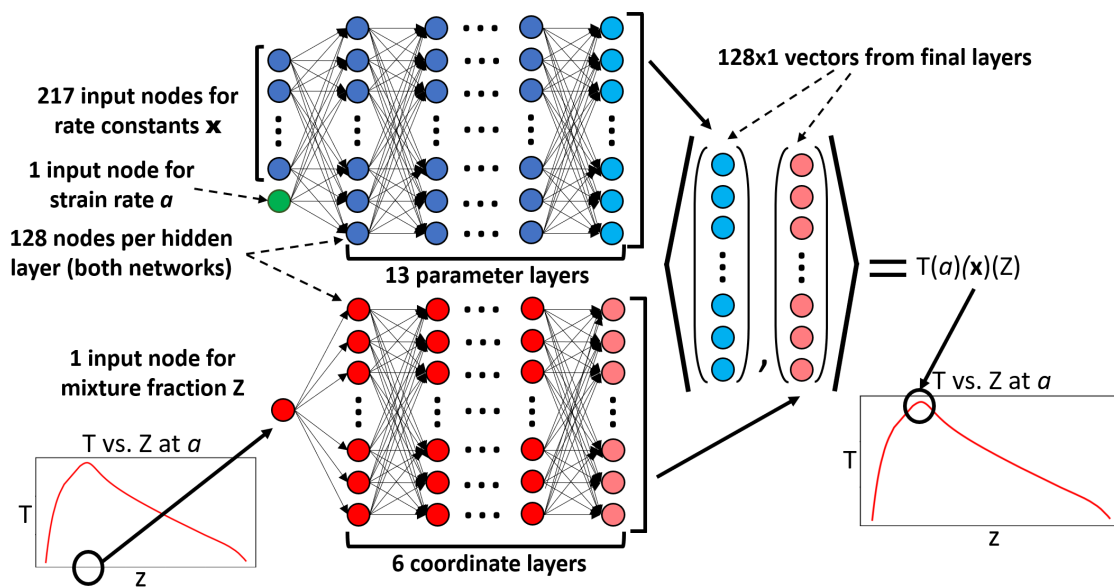

Figure 2-2: Neural network surrogate model for flamelet simulations to accelerate sensitivity computations. The parameter and coordinate branches are independent until the last layer in which their results are combined via inner product to arrive at a final temperature prediction. Residual skip connections every two layers are not shown to maintain clarity. Training occurs independently of discretization, and the network can be evaluated on any inputs Z and a in an arbitrary grid.

The hyperparameters of this network were selected using the Ray Tune package [61], which as implemented here performed a grid search throughout reasonable ranges of hyperparameters to identify the network that performed best during initial

epochs. The highest-performing hyperparameter set identified using this package was implemented for the single network used in downstream training until convergence. This final network comprised 13 parameter layers and 6 coordinate layers of 128 nodes each. The learning rate and batch size were $1.1 \cdot 10^{-4}$ and 256, respectively. Residual skip connections [62] every two layers were used in both sub-networks to reduce any impacts of depth-based performance degradation. Sigmoid-weighted linear units [63] were used as activation functions, and the ADAM optimizer [64] with a weight decay of $1 \cdot 10^{-4}$ was used to update the network parameters.

2.2.2   Training Data Generation

Flamelet solution training data was generated using the GRI-Mech 3.0 detailed kinetic mechanism [53], in a truncated form neglecting NOx chemistry with 217 reactions. This widely referenced and applied mechanism is the result of optimization across extensive experimental datasets, though due to the inherent complexity in these chemical reaction kinetics its parameters still contain significant uncertainty. These uncertainty ranges were adapted from a separate work [54], and as detailed in Eq. 2.1 define the range of $\mathbf{x}$ in which the kinetic parameters are sampled. With this mechanism and the corresponding uncertainty ranges, the flamelet computations were carried out in Cantera [52] in the counterflow configuration using fuel composition and temperature boundary conditions that match the turbulent case (discussed in Section 2.3) to facilitate later application directly in the turbulent flamelet model. Datasets were computed across a large range of strain rates (defined here using the formulation in Eq. 2.2) from $3 \cdot 10^{-2}$ 1/s to near extinction at $3 \cdot 10^{2}$ 1/s. Scaling rules for rapid convergence across the strain rate coordinate were taken from [65], leading to a variably sized physical domain width D and mass fluxes on the fuel and oxidizer side $\dot{m}_{f/o}$ as the strain rate was increased toward extinction over iterations i,

$$D_{i+1} = D_i \left(\frac{a_{i+1}}{a_i}\right)^{-1/2},$$
$$\dot{m}_{f/o,i+1} = \dot{m}_{f/o,i} \left(\frac{a_{i+1}}{a_i}\right)^{1/2}. \tag{2.10}$$

Finally, with gradients evaluated in a trained neural network surrogate model and the active subspace algorithm as described in Eqs. 2.8 and 2.9, the r_u-dimensional subspace that is applied to propagate kinetic uncertainty forward through the turbulent nonpremixed combustion simulation described in Section 2.3 can be computed.

2.3   Benchmark Turbulent Flame Simulation Details

Under the conditions outlined in Section 1.2.2, the interaction between the turbulence and chemistry in a turbulent flame can be modeled using the steady laminar flamelet approach. This enables direct application of the kinetic uncertainty information discovered in Section 2.1 to a turbulent case without the need to repeat the initial reduction process. The initial reduction process samples flamelets in the full, 217-dimensional space, while forward propagation of the turbulent flame within the subspace requires only sampling in the $r_u << 217$-dimensional space, indicating the computational savings attached to this physics-based abstraction of uncertainty. This section details the flamelet-based turbulent combustion simulation used in this work to first evaluate the multi-target performance of the methodology in Section 2.1, and then apply it for extremely efficient uncertainty quantification.

A two-dimensional axisymmetric model of the piloted Sandia Flame D [66], a commonly referenced nonpremixed turbulent combustion benchmark, was used to evaluate the applicability of the flamelet-derived subspace to a multidimensional turbulent simulation. This configuration involves a $7.2 \cdot 10^{-3}$ m diameter partially premixed fuel jet of 25% methane and 75% dry air (by volume) surrounded by an $18.4 \cdot 10^{-3}$ m pilot of hot combustion products (taken as Z=0.27 as per [67]), with an outer co-flow of cold air. The velocities of these three flows are 49.6 m/s, 11.4 m/s, and 0.9 m/s, respectively. The inlet temperatures are 294 K, 1880 K, and 291 K, respectively. The final mesh used to investigate the forward problem, as well as a general description of the computational domain, is shown in Fig. 2-3.

A standard, straightforward, and relatively inexpensive model was developed for application in forward uncertainty propagation leveraging various previously exam-

ined and verified methods for the Sandia Flame D [68, 69, 70]. A stretched grid of 24,180 cells (Fig. 2-3) is used to discretize the 1.2 m × 0.3 m computational domain. The flame is simulated using the realizable $k - \epsilon$ model. The realizable model differs from the standard $k - \epsilon$ model in its formulation of the dissipation rate and eddy viscosity equations, and was originally proposed and later applied to the Sandia Flame D [68, 71] for its improved spreading rate performance in axisymmetric jet flame simulations. Following the flamelet-based uncertainty method (and similarly to [69]), the steady laminar diffusion flamelet model with unity lewis numbers is used for the turbulence-chemistry interaction, along with the GRI-Mech 3.0 mechanism [53]. This model parameterizes flamelets uniquely using the mixture fraction and scalar dissipation rate at the stoichiometric mixture fraction. The latter is linearly related to the characteristic strain rate formulation defined in Eq. 2.2 through the following equation,

$$\chi_{st} = \frac{a}{\pi} exp(-2[erf^{-1}(1 - 2Z_{st})]^2), \tag{2.11}$$

where χ_{st} is the instantaneous scalar dissipation rate at the stoichiometric mixture fraction Z_{st} and a is the strain rate defined identically as in Eq. 2.2. This direct relationship between the kinetically investigated flamelet phase space and the turbulent simulation's flamelet table coordinates allows for uncertain solutions that are theoretically directly coupled to information contained in the subspaces discovered from the (a, Z) flamelet table used in Section 2.1. Detailed discussion of the model formulations are available in [72], while validation of the current simulation results is provided in Section 3.3.
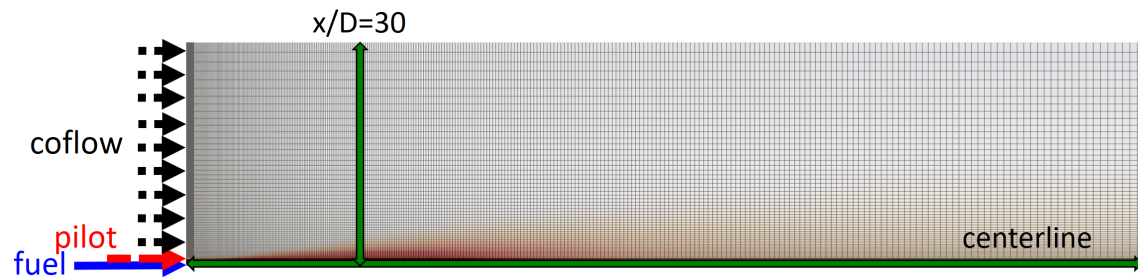
Figure 2-3: Stretched axisymmetric computational mesh used for Sandia Flame D simluations, with nominal temperature profile overlaid in red for visualization. Green arrows in mesh show profile sampling locations used for forward propagation visualization and metrics in Figs. 3-11, 3-12, and 3-13.

Chapter 3

Results

This section begins with a presentation of the training results of the neural network surrogate model. Then, the active subspace reduction process is demonstrated on a methane flamelet table. This is accompanied by discussion of the dependence of not only the subspace directions but also the key sensitive reactions on the location in the flamelet table phase space, necessitating the extended multi-target approach used in this work. Next, validation is shown for the turbulent simulation used for forward uncertainty propagation, both in mesh refinement consistency and in consistency with experimental and computational results from the literature. Following this is a presentation of the turbulent simulation uncertainty's dependence on the various subspace directions, specifically in its substantial variation when evaluated at different locations in the turbulent combustion simulation domain. Discussion here highlights the versatility of the multi-target subspace generation process in capturing these variations in kinetic uncertainty response. Finally, the results of the subspace-enabled efficient forward uncertainty propagation in the turbulent simulation are presented, and the accuracy of these results is compared against the estimated ground truth.

3.1 Active Subspace Methodology

3.1.1 Neural Network Training Results

Recalling that a neural network surrogate model trained on perturbed flamelet so-
lutions in Cantera is used to accelerate the kinetic reduction, the trained network's
performance is reported in Fig. 3-1 through a comparison between the network-
generated solutions and Cantera solutions for out-of-sample testing cases at various
strain rates spanning three orders of magnitude. The agreement is very strong over-
all, with the highest observable error occurring near the fuel inlet for the low strain
case, and near the peak temperature region for the highly strained case. These results
were deemed sufficient to proceed with the active subspace discovery process in the
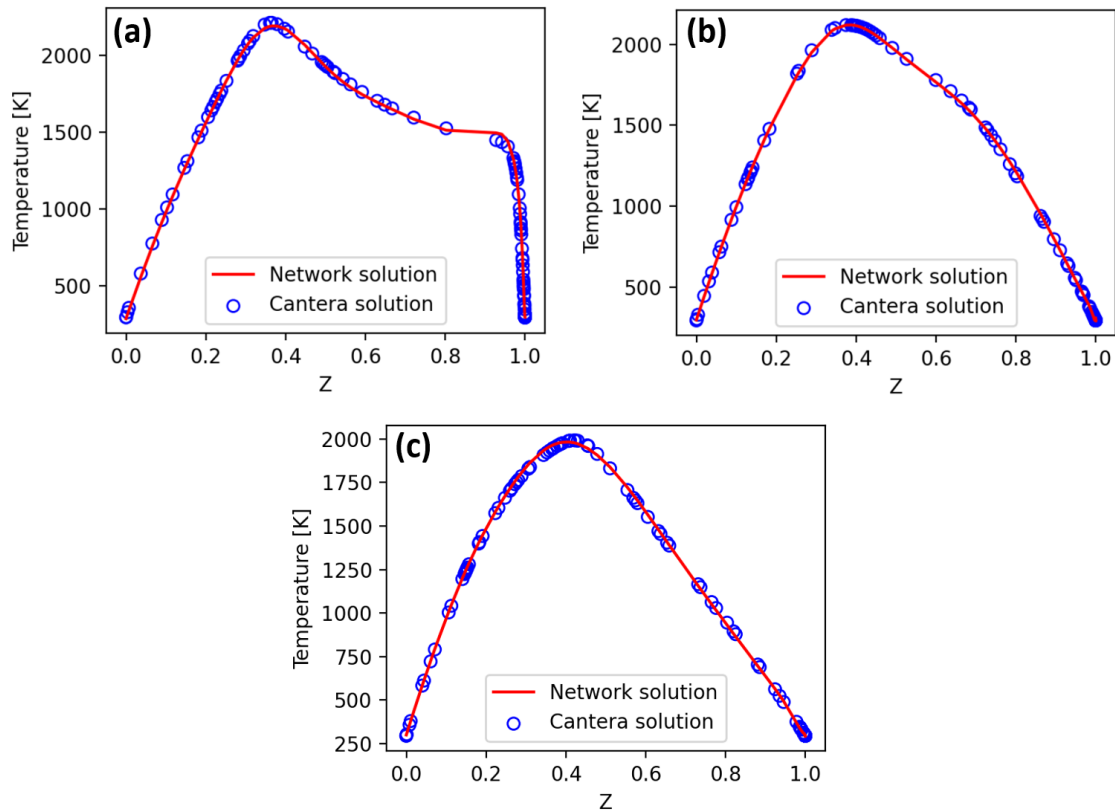following section.

Figure 3-1: Network temperature evaluation on the out-of-sample testing data at the
end of the training, shown for a broad range of strain rates across three orders of
magnitude: **(a)** 0.088 s^{-1}, **(b)** 3.3 s^{-1}, and **(c)** 93 s^{-1}.

3.1.2   Active Subspace Computation

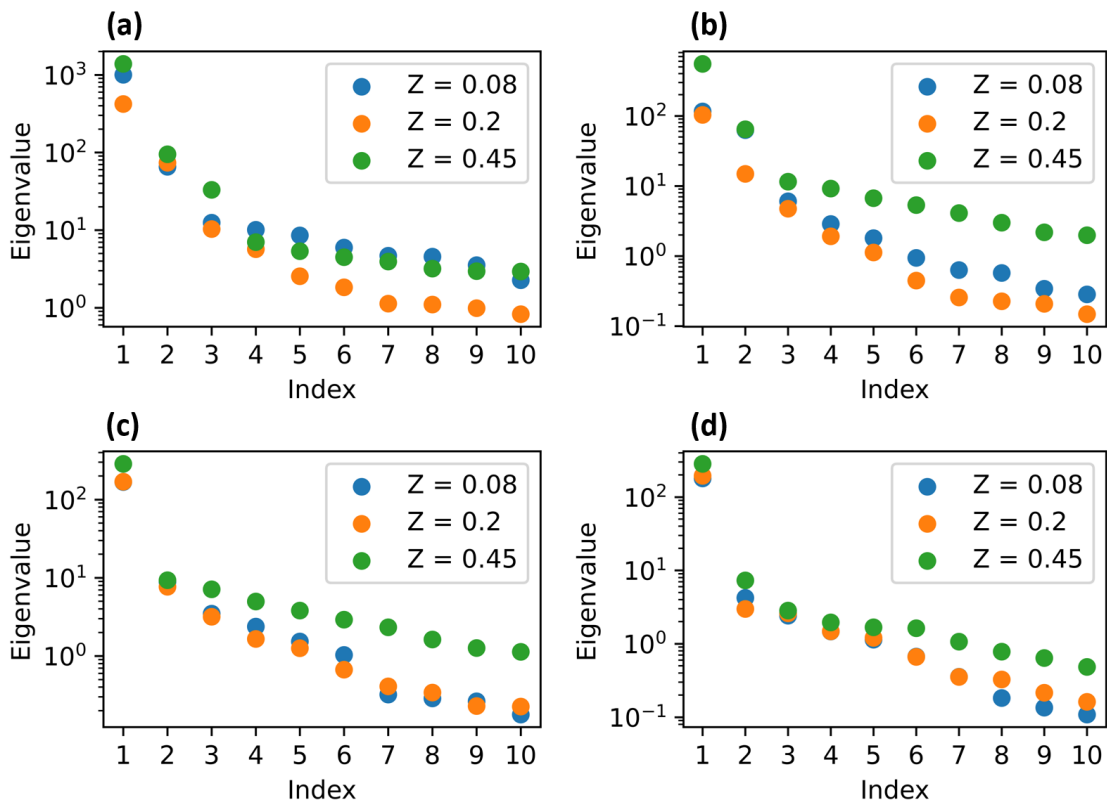**Local Subspaces in Flamelet Table**

Figure 3-2: Eigenvalues from the first subspace reduction of Eq. 2.8, plotted at various strain rates spaced roughly uniformly in log space from **(a)** low to **(d)** near extinction. Each subplot has three scatter colors corresponding to three locations in the flame at fuel, oxidizer, and stoichiometric locations. 1-D behavior is seen across all mixture fractions at the higher strain rates, but not at the lower strain rates.

The inexpensive gradient evaluations provided by the trained neural network are used to implement the kinetic subspace discovery algorithm outlined in Section 2.1. Eq. 2.8 is first evaluated once at each mixture fraction and strain rate pair (a, Z) using 500 kinetically perturbed gradient samples. The eigenvalues of these single-target reductions can be plotted to identify the drop-off point, from which the dimension of the reduced subspace can be determined. Fig. 3-2 includes plots showing the eigenvalues at various (a, Z) locations in the flamelet table, where each subplot is at a fixed strain rate and includes eigenvalues at fuel side, oxidizer side, and stoichiometric

mixture fractions. Figs. 3-2c and 3-2d were taken from higher strain rates and have behavior similar to that of [51], where strong 1-D behavior can be inferred from the sharp dropoff of greater than an order of magnitude at all mixture fractions between the first and second eigenvalues. Figs. 3-2a and 3-2b, however, at the lower strain rates which were not investigated in [51], do not indicate one-dimensional behavior as strongly. In certain cases, such as on the oxidizer side of Fig. 3-2b, there is a nearly indistinguishable difference in magnitude between the first and second eigenvalues, and a more convincing dropoff between the second and third.

As discussed in Section 2.1, the multidimensional behavior of certain (a, Z)-local subspaces is neglected in the remainder of this work. A strong majority of subspaces appear to indicate one-dimensional behavior (as will be shown later in Fig. 3-6), and it was found in heuristic testing that the uniformly applied one-dimensional assumption provides the most accurate final subspaces. This may be an area for further optimization and refinement in future applications of the methodology, but is not considered in this work for the initial development and demonstration.
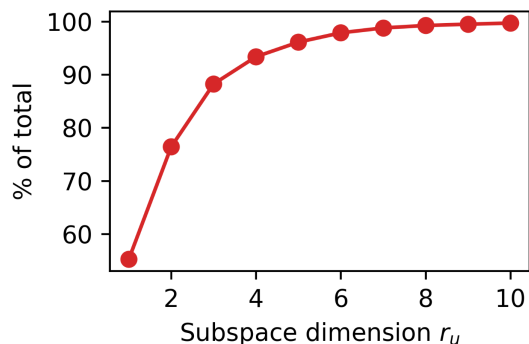
Global subspace across Flamelet Table

Figure 3-3: Percentage of variance across all local subspaces captured by global subspaces with variable dimension r_u, computed through the percentage of all squares of singular values of $\mathbf{A}$ contained in the sum up to a given index. Here, $r_u = 3$ is selected for 88% accuracy to the local subspaces.

After having found the series of (a, Z)-local subspaces using Eq. 2.8, the SVD in Eq. 2.9 is used to reduce this set globally across the entire flamelet table. The singular

value magnitude analysis is similar to the analysis attached to Eq. 2.8, though is now carried out more carefully in order to select the best low-dimensional subspace for downstream application in the turbulent combustion simulation. The percentage of local subspace information captured by various sizes of global subspace, computed using the square of the singular values, is reported in Fig. 3-3. A percentage of 100 at r_u would indicate that subspace variation across $\mathbf{A}$ could be represented entirely by the set of directions up to r_u. Here, $r_u = 3$ was chosen for the remainder of this work to compromise between more directions for high accuracy and fewer directions for efficient forward propagation. This selection can be tailored in future applications based on the needs of the user. For example, in a high-cost turbulent simulation, one may want to reduce even further to two dimensions, sacrificing minor accuracy for even more efficient large-scale sampling. In contrast, in a lower-cost simulation where such a compact representation is not as important and perhaps high accuracy is more desirable, the number of dimensions could be brought up closer to $r_u = 10$, where the accuracy begins to converge above 99%.

3.1.3 Global Subspace Directions and Metrics

At this point, the multi-target, low-dimensional subspace to be used in the forward propagation of kinetic uncertainty through the turbulent combustion simulation of Section 3.5 has been identified. The remainder of the current subsection involves a detailed report of the kinetic composition of the identified three-dimensional global subspace, as well as a verification of its performance in efficiently predicting the uncertainty response of the flamelet table, which can serve as an indicator of accuracy in the full-scale turbulent simulation.

In Fig. 3-4, the kinetic components of the final three subspace directions are plotted, as well as the activity scores based on the SVD of Eq. 2.9. These activity scores were computed using the following equation adapted from [38],

$$\alpha_\ell = \sum_{m=1}^{d} \sigma_m^2 w_{m,\ell}^2, \qquad (3.1)$$

41

where the activity score α for each reaction ℓ is the sum of the square of the non-truncated subspace components $\mathbf{w}_{m,\ell}$, weighted by the corresponding squared singular value σ_m^2. Fairly rigorous mathematical and simulation-based verification in [38] supports the use of activity scores as a global sensitivity metric. This concept is leveraged in Section 3.2 to emphasize a major advantage of the active subspace approach when compared to traditional sensitivity analysis-based reaction perturbations.
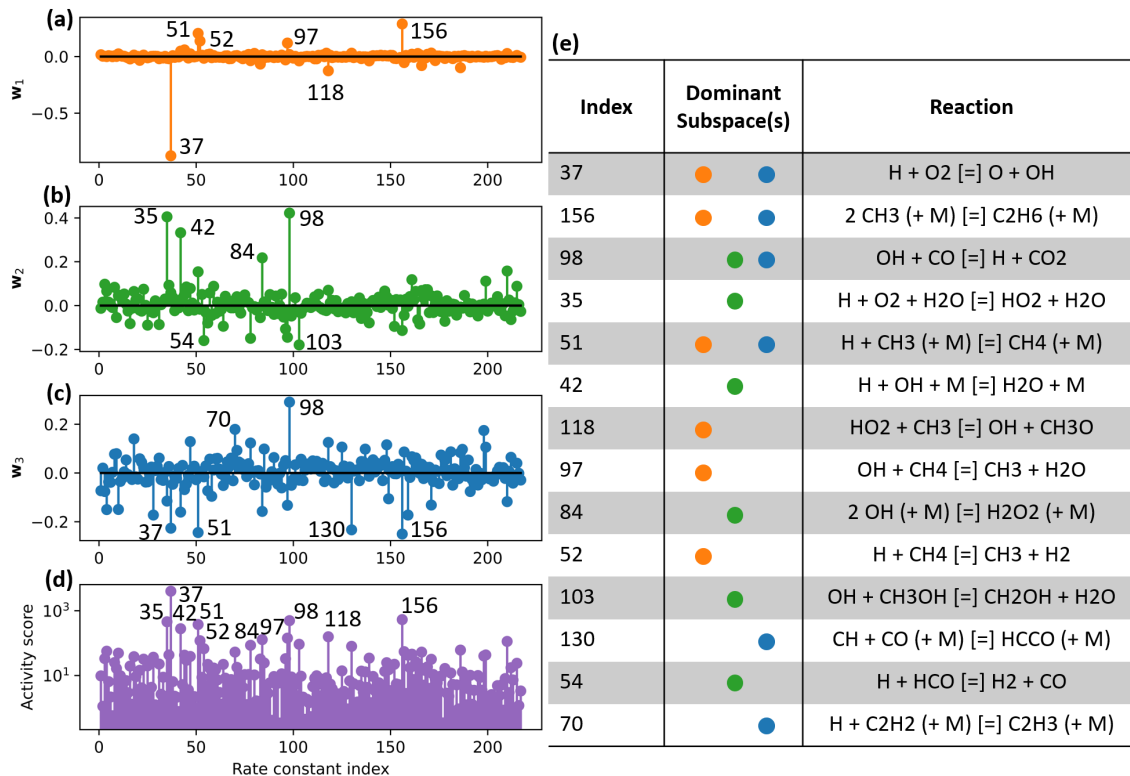

Figure 3-4: Kinetic analysis based on the first three global subspace directions and activity scores. **(a)** $\mathbf{w}_1$, **(b)** $\mathbf{w}_2$, **(c)** $\mathbf{w}_3$, and **(d)** activity scores. The top six reactions in each direction are labeled in subspace direction plots, and the top ten overall sensitive reactions are labeled in the activity score plot. **(e)**: Reactions corresponding to each index labeled in **(a-d)**, in order of activity score. Dominant subspaces are reported according to the labeled reactions in **(a-c)**. Only four reactions appear in these rankings for more than one subspace and none appear in all three, indicating the relatively large set of sensitive reactions spread over these three subspace directions.

Next, the accuracy of this three-dimensional subspace in predicting the temperature uncertainty in the flamelets is investigated. The same methodology as is used in [51] is applied to compare perturbed flamelet solution profiles in the subspace against those in the full kinetic parameter spaces, using the percent error between

the temperature uncertainty profiles to gauge the accuracy of the subspace. At each subspace location, 500 kinetic uncertainty samples $\mathbf{b}_{d,j}$ are drawn from the full kinetic uncertainty space, with j ranging from 1 to 500. These samples are solved forward in Cantera for uncertainty ranges on the temperature profiles. Then, they are projected into the subspace directions $\mathbf{w}$ as per

$$\mathbf{b}_{r_u,j} = \sum_{k=1}^{r_u} [(\mathbf{b}_{d,j} \cdot \mathbf{v}_k)\mathbf{v}_k], \tag{3.2}$$

where $\mathbf{b}_{r_u,j}$ contains the same perturbation information as $\mathbf{b}_{d,j}$, expressed in reduced rank using the $r_u = 3$ basis vectors $\mathbf{w}_k$. This operation reduces each vector $\mathbf{b}_{d,j}$ to a linear combination of the three basis directions $\mathbf{w_k}$. From this linear combination it reconstructs parameter vectors of length d but rank $r_u = 3$ to test in Cantera. This enables comparison of temperature profiles based separately on the sets of vectors $\mathbf{b}_{r_u,j}$ and $\mathbf{b}_{d,j}$, to evaluate how much of the original information is captured by the r_u-rank sample. This step, performed in Cantera as opposed to the neural network surrogate model, also serves to verify that the surrogate model results were accurate and suitable for use in the subspace reduction.

The accuracies of these temperature profiles are plotted locally at each mixture fraction and strain rate in Fig. 3-5. At lower strains the three-dimensional subspace is not able to predict the temperature uncertainty as well as at higher strains. The overall accuracy here defined by mean absolute error is 85%, which corresponds fairly well to the 88% accuracy to the local subspaces that was predicted from Fig. 3-3, with a slight decrease likely due to the truncation to a single direction in the first reduction step at fixed (a, Z) values. These three subspace directions are thus sufficient to largely capture the temperature uncertainty in the flamelet table. Before moving onto the next step and applying this subspace in the scaled-up turbulent simulation, the following subsection first discusses irregularities in the uncertainty response across the flamelet table, which include certain unexpected dependences on strain rate, and the current method's advantage over traditional methods in handling such discrepancies.
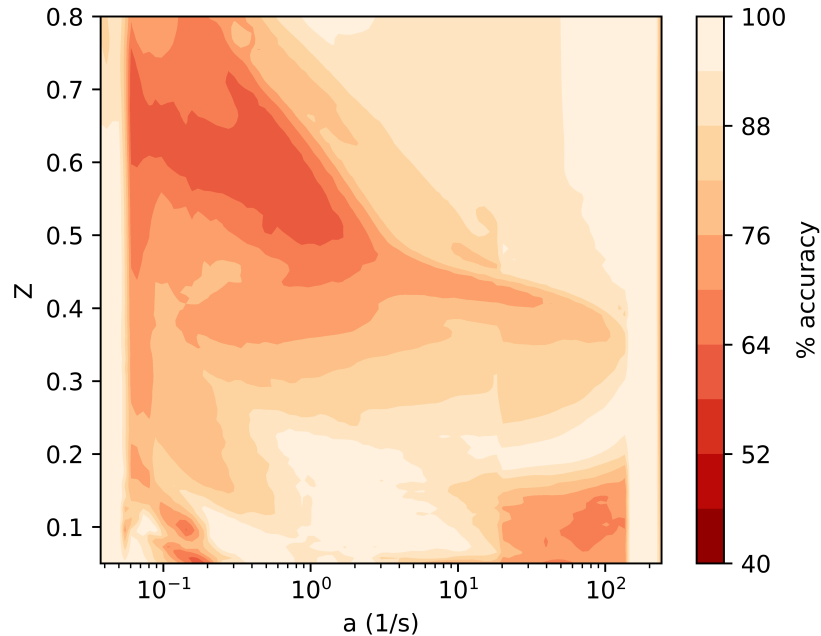
43

Figure 3-5: Accuracy of the three-dimensional global subspace at each local (a, Z) in the flamelet space, measured by agreement in uncertainty quantiles when compared to full-dimensional uncertainty ranges.

3.2 Necessity of a Multi-Target Subspace Approach

This section specifically details two key advantages of the multi-target subspace reduction detailed here, when compared first against traditional methods of sensitivity-based dimension reduction, and secondly against simpler zero or one-dimensional active subspace approaches.

3.2.1 Greater Dimension Compression

According to the activity scores of Fig. 3-4, R37 is the most important reaction for the forward propagation of uncertainty. However, it fails to capture even half of the global temperature variance as defined by the activity score. The next four reactions each contain between four and six percent of the total variance, with a further seven capturing between one and three percent each. In fact, it takes the set of the thirteen most sensitive reactions to even capture 75% of the total variance present across the flamelet table. In contrast, the active subspace method's exploration of sensitivity

directions instead of sensitivity indices allows for greater compression of information. It is seen that the first active subspace direction $\mathbf{w}_1$ is largely dominated by the key R37, but that the second and third directions $\mathbf{w}_2$ and $\mathbf{w}_3$ contain perturbations of many of the remaining key reactions compressed into fewer sensitivity directions. While perturbing these sensitive reactions themselves would require the exploration of a kinetic space of dimension greater than ten in order to achieve fair accuracy, with just three active subspace directions it is possible to very efficiently explore the same uncertainty space with fewer required turbulent simulations.

A similar conclusion can alternatively be drawn from closer inspection of the key sensitive reactions across the local subspaces. The shifts there in kinetic sensitivity direction do not simply amount to a reshuffling of a fixed group of key reactions, but instead indicate both a change in direction and a change in key reaction indices. A detailed visualization of this phenomenon is provided in the appendices. Fig. B-1 indicates five sampling locations in the flamelet table, precise coordinates of which are given in Table A.1. Table A.2 and Fig. B-2 show the high dissimilarity of kinetic sensitivity across these five locations both in sensitivity direction and in highly sensitive reactions. It can thus be inferred both from the global subspace across the entire flamelet table as well as from the local subspaces within the flamelet table that there are substantially more sensitive reactions than there are sensitive directions of reactions, a phenomenon that the active subspace algorithm takes advantage of in its greatly compressed yet still highly accurate vector-based representation of the kinetic uncertainty.

3.2.2 Dependence of Kinetic Sensitivity on Flamelet Parameters

Next, the strain dependence of the local kinetic subspaces is investigated, now entirely within the frame of kinetic directions (in contrast to the direction vs. index discussion in Section 3.2.1). It was found in [51] that these local subspaces varied strongly across the mixture fraction space of a single flamelet, which originally motivated the
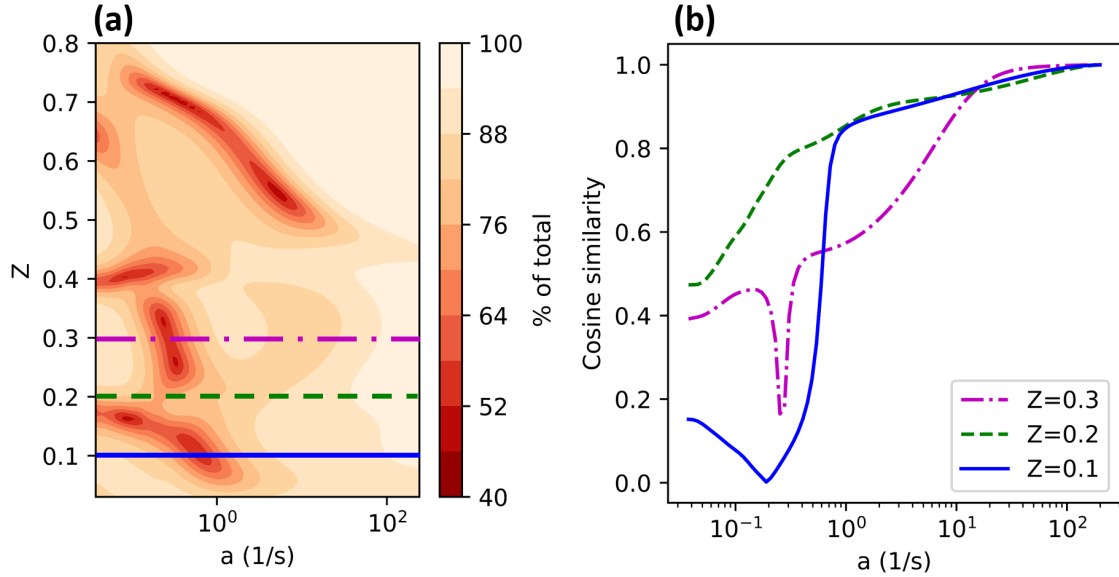
Figure 3-6: **(a)** Percent of sum of all eigenvalues represented by the first eigenvalue from Eq. 2.8, describing the variation in gradient information that can be captured by a single subspace direction at each (a, Z) coordinate in the flamelet table. **(b)** Strain dependence of the cosine similarity of local kinetic subspaces at three sampled mixture fractions when compared to the near-extinction strain rate. Values near unity are observed in the high-strain region, while as the strain is further reduced the kinetic similarities decrease substantially.

SVD from Eq. 2.9 for the construction of a global subspace. The authors of that work cited the result of [73], which showed that kinetic sensitivity directions did not change with strain rate, and proposed that their subspace constructed from a flamelet at a highly strained condition might apply across the entire flamelet table. Reported here are various strain rate-dependent local subspace quantities in Fig. 3-6 to test this hypothesis. In Fig. 3-6a, as the strain rate moves away from the extinction value, it is seen to become more and more difficult to capture a significant portion of the local sensitivity information in a single subspace direction. The difference in the exact shape of this result and that of Fig. 3-5 is likely due to shared information or a lack thereof across subsets of the (a, Z) domain - that is, the existence of local one-dimensional subspaces across a swath of the domain does not imply similarity across such one-dimensional subspaces, and conversely a swath of the domain with poor one-dimensional behavior does not necessarily imply the dissimilarity of these

multidimensional subspaces. Such discrepancies are evident in Fig. 3-6b when comparing the fuel-rich slice against the stoichiometric and lean slices at mid-range strain rates. Further analysis of Fig. 3-6b confirms certain strain-dependent phenomena. There, the kinetic similarity is seen to be preserved fairly well in the highly strained $a \sim 30 - 300s^{-1}$ range leading up to extinction, corroborating the conclusion of [73] that for near-extinction flamelets the kinetic sensitivity does not depend on the strain rate. Below this point, however, as samples are taken toward the lower strain rates that were not considered in [73], the similarity in kinetic sensitivity is seen to break down at all three sampled mixture fractions - stoichiometric, fuel side, and oxidizer side. Thus the similarity result of [73] and the corresponding discussion in [51] appear to remain valid in the high strain rate regimes investigated in those works, and break down as the target is moved into significantly lower strain rates. It is this breakdown of similarity that calls for the two-dimensional reduction step detailed in Section 2.1.2, as opposed to the one-dimensional reduction of [51] (or the zero-dimensional process typically used in the literature).

Separate from the strain dependence of the subspace directions is the question of locally one-dimensional behavior. In Fig. 3-6a, the percentage of the full sum of eigenvalues captured by the first index drops to nearly as low as 40%. This result, combined with the lack of convincing one-dimensional behavior seen in certain corresponding cases in Fig. 3-2, indicate that there likely does not exist a one-dimensional local subspace at certain (a, Z) locations in the flamelet table. The choice of uniformly one-dimensional subspaces was justified fairly rigorously in the high-strain case of [51], though in the transition to include all strained cases in this work, this justification no longer holds. Regardless, heuristic accuracy testing using various combinations of one and two-dimensional subspaces found that the one-dimensional assumption, even in the updated, strain-dependent case, provides the highest accuracy when applied in the turbulent simulation. Based on this, higher dimensional local subspaces were not considered in this work, though further optimization in this area may be a useful target for future development.
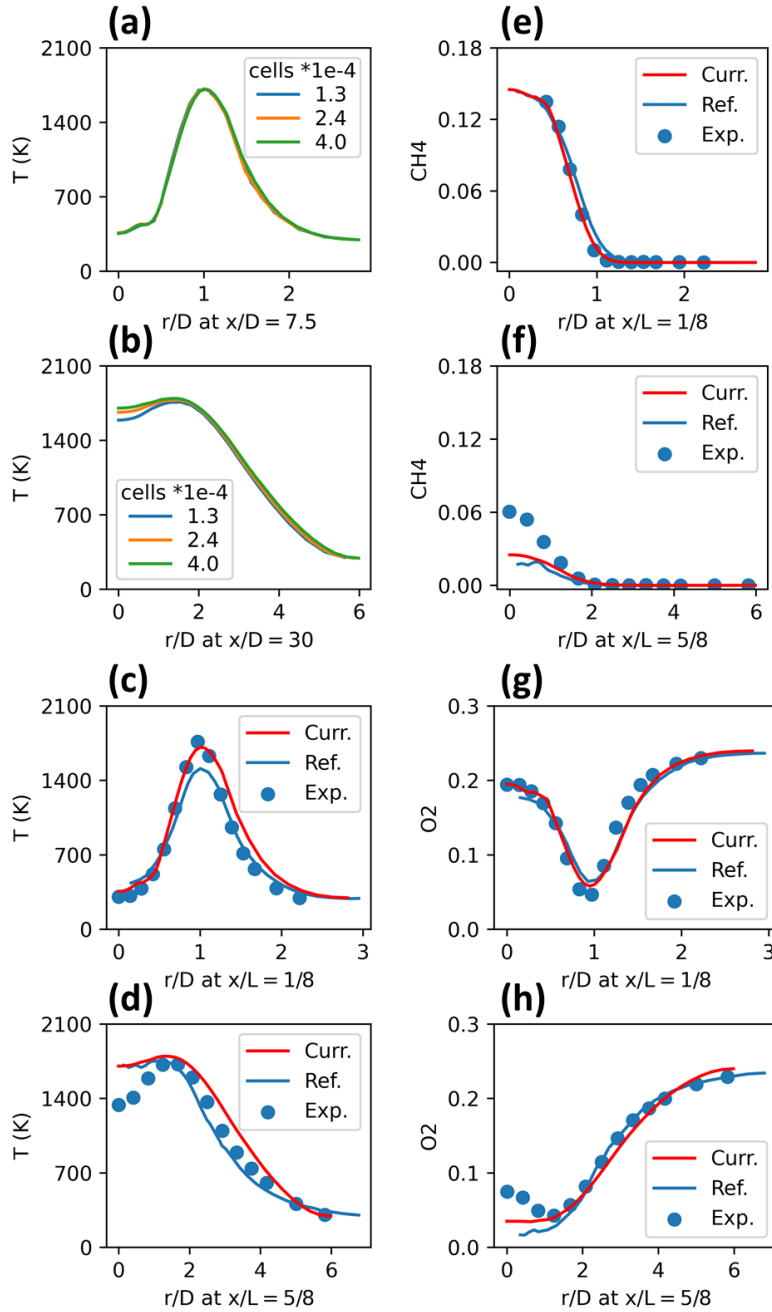
3.3   Turbulent Simulation Validation

Figure 3-7: Validation of the current Sandia Flame D simulation. **(a-b)** Grid convergence results of temperature slices at $x/D = 7.5$ and $x/D = 30$ on top and bottom, respectively. 24,180 cells used henceforth. **(c-h)** Validation against computational [69] and experimental [74] results in the literature for **(c-d)** temperature, **(e-f)** methane mass fractions, and **(g-h)** oxygen mass fractions.

This section presents validation of the turbulent combustion simulation used in this work for forward uncertainty propagation and subspace performance evaluation. The mesh size is evaluated through the refinement test in Fig. 3-7a-b, where strong consistency in the temperature values is observed as the mesh is refined at two slices in the simulation domain. These results motivate the selection of 24,180 cells for use in downstream validation and testing. After having selected the final mesh size, converged results were then verified against the model results of [69] and the experimental data of [74], in Figs. 3-7c through 3-7h. The goal of the validation in this case is not to outperform the existing computational model of [69], as this work does not present any novel developments in turbulent combustion simulation. Instead, the goal is simply to create a model that reasonably replicates prior computational studies as well as real-world experimental data. The comparisons in Fig. 3-7 show this well, with the current result largely matching up well to the previous computational study, the experimental data, or both. At this point, with the simulation demonstrated to be consistent with itself and with the literature, the three-dimensional subspace's performance can be examined through its scaling up from the flamelet table to the more complex turbulent flame.

3.4 Spatial Dependence of Kinetic Sensitivity in Turbulent Flame

With a finalized three-dimensional kinetic subspace and a verified turbulent model, the next step involves analysis of the spatial variation of kinetic sensitivity directions in the turbulent flame. This section serves to confirm key results of Section 3.1, and the proposed highly efficient forward propagation is not discussed until Section 3.5. To begin, a baseline result is established by sampling the full-scale uncertain kinetics and generating solution profiles for 2,000 kinetic perturbations. The statistics have not yet fully converged with 2,000 samples, though to save on computational effort the result found in [16] is referenced, where 2,000 flamelet samples was reported as

a lower bound for good performance in the same physical problem with a similar flamelet model and an identical chemical reaction mechanism. These samples are not required for the proposed subspace-powered forward uncertainty quantification in the turbulent simulation. They instead serve to help visualize how the uncertainty in the full kinetic space reacts to each subspace, and propose accuracy values for the efficient subspace-driven forward uncertainty solutions shown later in Section 3.5. Thus, the general value of 2,000 samples is taken at face value here without rigorous testing. The type of detailed spatial analysis and accuracy prediction presented here was not possible in [16] due to the more accurate and more expensive large eddy simulations used, as well as the previously discussed difference in approach to kinetic reduction.

The summary plots in Fig. 3-8 show how the maximum temperature at the centerline and maximum temperature at the near-nozzle $x/D = 30$ slice in the turbulent simulation change with motion along the three subspace directions. A perfect one-to-one functional mapping of temperatures to motion along a subspace direction would indicate that such a one-dimensional subspace is able to fully explain all of the target temperature variation, regardless of motion along the other 216 kinetic directions contained in each sample. This is the expected result for a perfect one-dimensional subspace. Conversely, an uncorrelated, cloud-like shape in such a mapping indicates that those other 216 kinetic directions substantially affect the temperature response, and thus the investigated subspace direction is not able to unilaterally predict the temperature response well or even at all. Inspection of the two-dimensional summary plots, moving from the top toward the bottom, reveals that the centerline maximum temperature is not correlated with movement in direction $\mathbf{w}_1$, which is fairly surprising given the relative dominance of that subspace direction from Fig. 3-3. Conversely, the response of the maximum temperature of the near-nozzle slice responds extremely well to $\mathbf{w}_1$. Both temperatures respond fairly well to $\mathbf{w}_2$, though the centerline temperature has a tighter spread and can thus be said to more closely align with motion in the $\mathbf{w}_2$ direction. The centerline temperature responds fairly strongly to $\mathbf{w}_3$, while the near-nozzle slice has a much weaker and interestingly inverse relationship with $\mathbf{w}_3$. Finally, when the strongest pair of subspaces is chosen for the bottom set of Fig.
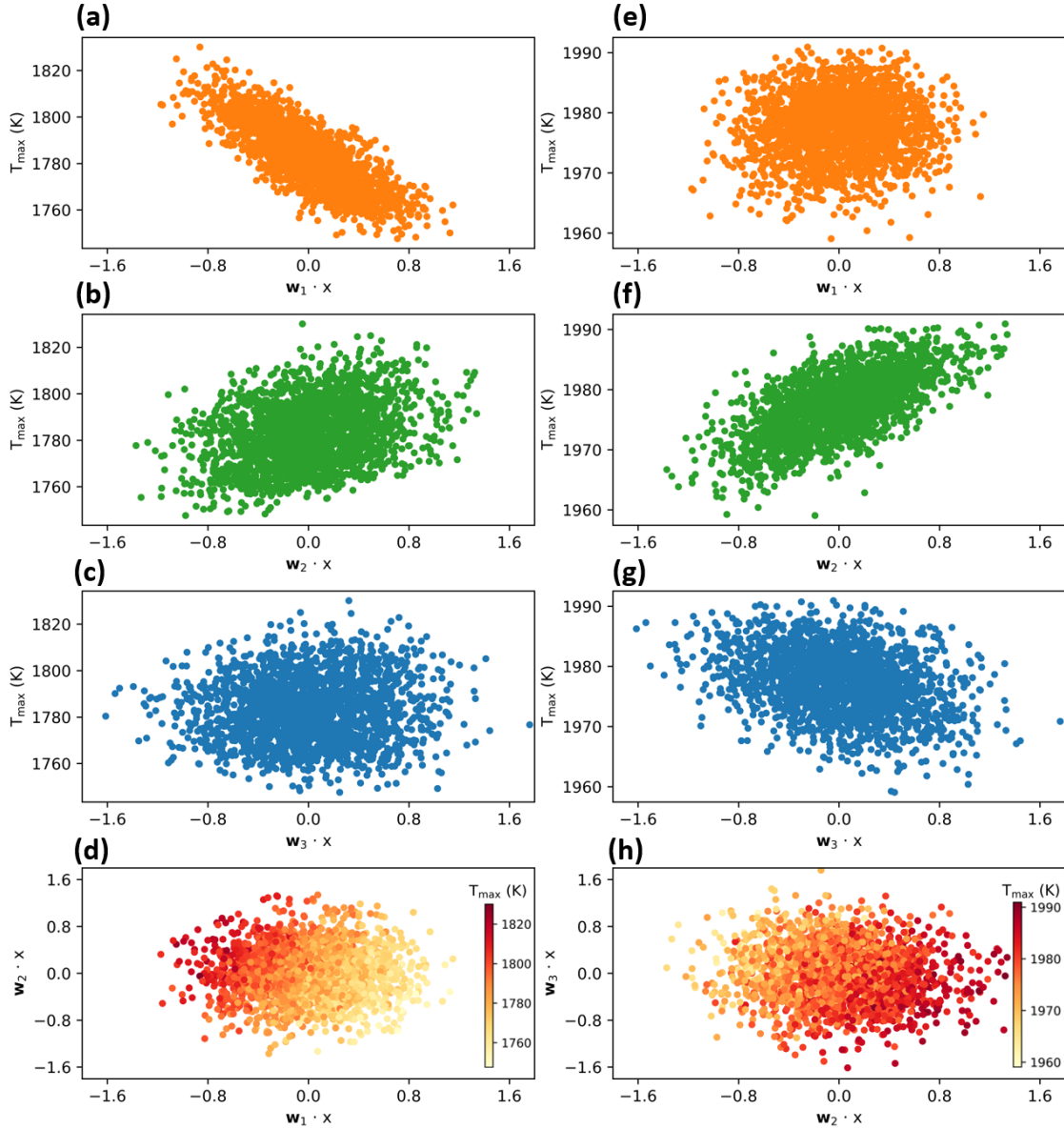
Figure 3-8: Summary plots showing the response of **(a-c)** the near-nozzle ($x/D = 30$) maximum temperature and **(e-g)** the centerline maximum temperature to motion along the $\mathbf{w}_1$, $\mathbf{w}_2$, and $\mathbf{w}_3$ subspace directions, respectively. **(d)** and **(h)** show coupled responses of the same temperature values to motion along two subspace directions. Based on the substantial shifts in the dominant subspace directions seen across each pair in the top six subplots, the axes in **(d)** and **(h)** are $\mathbf{w}_2$ vs. $\mathbf{w}_1$ and $\mathbf{w}_3$ vs. $\mathbf{w}_2$, respectively.

3-8 plots showing temperature responses to coupled inputs, two-dimensional behavior is observed in both cases. Notably, the meaningful two-dimensional behavior is observed in $\mathbf{w}_2$ and $\mathbf{w}_3$ for the centerline maximum temperature and conversely $\mathbf{w}_1$ and

$\mathbf{w}_2$ for the near-nozzle maximum temperature, following from the above discussion, and the two-dimensional trend appears to be more consistent in the near-nozzle case of Fig. 3-8d.
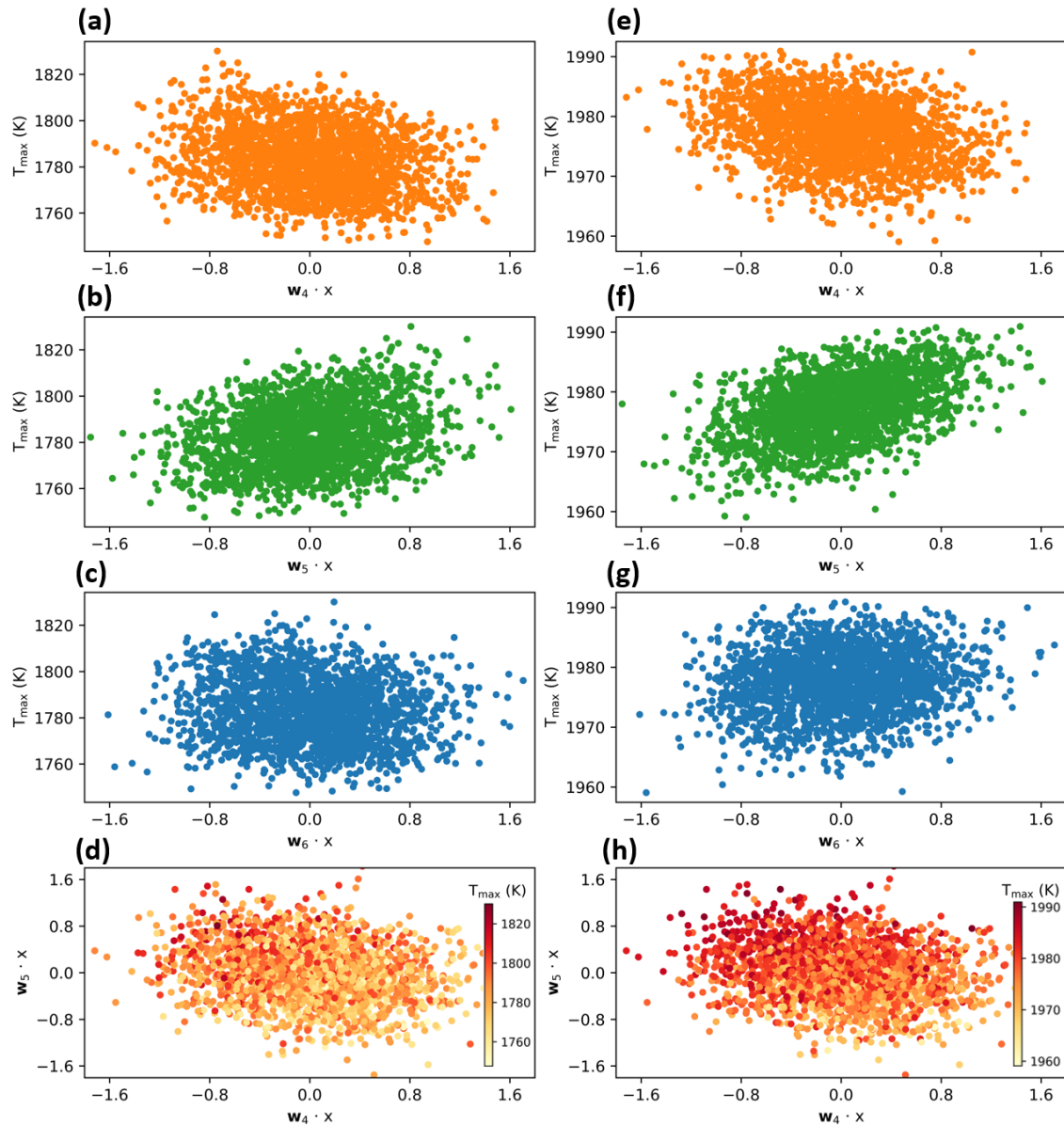

Figure 3-9: Summary plots showing the response of **(a-c)** the near-nozzle $(x/D = 30)$ maximum temperature and **(e-g)** the centerline maximum temperature to motion along the $\mathbf{w}_4$, $\mathbf{w}_5$, and $\mathbf{w}_6$ subspace directions, respectively. **(d)** and **(h)** show coupled responses of the same temperature values to motion along $\mathbf{w}_4$ and $\mathbf{w}_5$.

In addition to Fig. 3-8, which shows the summary plot responses of maximum temperatures to the three kinetic subspace directions selected for downstream forward

propagation, it is additionally interesting to investigate the summary plots of the next three kinetic subspace directions, $\mathbf{w}_4$ through $\mathbf{w}_6$. Based on the truncation in Fig. 3-3, these are the most important directions not included in the selected $\mathbf{w}_1$ through $\mathbf{w}_3$, and thus are in theory most indicative of the information lost in that truncation. In the left hand side column of Fig. 3-9, only weak correlations can be seen between the near-nozzle maximum temperature and $\mathbf{w}_4$ or $\mathbf{w}_5$, while $\mathbf{w}_6$ indicates no visible dependence at all. When plotting the temperature responses in two dimensions to the two most important of these directions, $\mathbf{w}_4$ and $\mathbf{w}_5$, it is similarly difficult to decipher any global trends. In contrast, the centerline maximum temperatures in the right hand side column of Fig. 3-9 appear to respond more substantially to these three directions. $\mathbf{w}_4$ and $\mathbf{w}_6$ in this case both have weakly visible trends, while $\mathbf{w}_5$ shows a more noticeable dependence. As expected, none of them show trends as tight and linear as that of $\mathbf{w}_2$. Overall, the contrasting results of Fig. 3-9, when compared against those of Fig. 3-8, demonstrate the dimension reduction capability and remarkably low-dimensional uncertainty representation enabled by the active subspace technique, even when applied in such a generalized manner.

The key takeaway from these summary plots is that the kinetic dissimilarity noted in the flamelet mixture fraction space in [51] as well as in the strain rate space in Fig. 3-6 appears to substantially propagate forward to the turbulent combustion simulation. When sampling near the nozzle, the maximum temperature's responses are strongly coupled to $\mathbf{w}_1$, which based on Fig. 3-4 is dominated by R37. Further downstream, however, this dependence appears to become nearly negligible, and the maximum temperature response is instead tied strongly to $\mathbf{w}_2$ and $\mathbf{w}_3$, which are made up of linear combinations of a much more diverse set of reactions. This spatially dependent result further highlights a drawback of the traditional, single-target combustion applications of the active subspace algorithm when the uncertainty target is a continuous profile and not simply a scalar value. Notable as well from the activity scores (in Fig. 3-4) is that there is no substantial overlap in key reactions across these three subspace directions. It is thus not simply a shifting dependence in a small set of key reactions that is observed, but instead a shift in the list of key reactions

themselves across the turbulent flame. This makes sensitivity index-based forward propagation more expensive due to the inflated number of sensitive reactions when considering the entire solution domain, an issue that is not observed here thanks to the greater dimensional compression offered by the active subspace.

3.5 Efficient Uncertainty Quantification of Turbulent Flame using Subspace

In this section, the accuracies of kinetic perturbations within the three-dimensional subspace are investigated when applied to the forward problem in the Sandia Flame D simulation. In the previous section, the need for greater than 2,000 samples in the full kinetic space in order to converge the statistics of the turbulent simulation was discussed. Here, samples are taken directly from the uncertainty space defined by the three-dimensional subspace (as opposed to the 217-dimensional full kinetic space). Special care is taken to preserve the literature-informed uncertainty ranges in this case. In the full uncertainty space, the distributions for each kinetic parameter are simply taken from [54], as per Eq. 2.1. In order to ensure that the subspace samples correspond to the information from [54], their normal distributions are informed by projections from the full space into the subspace. That is, similarly to how each reaction in the full space has its own uncertainty range as per Eq. 2.1, each subspace direction has its own unique uncertainty range defined by the projection of the collection of distributions in Eq. 2.1 into the three-dimensional subspace. The standard deviations of the three subspace directions vary up to 27% due to the variance in uncertainty across the detailed kinetic mechanism, and this additional step ensures that the subspace samples correspond both to the flamelet-informed kinetic uncertainty directions, as well as the literature-informed upper and lower bounds of such directions. These projections are visualized in Fig. 3-10, a histogram-based comparison between 2000 full kinetic samples projected into the subspace and 100 subspace-informed kinetic samples (drawn here solely to illustrate this point).
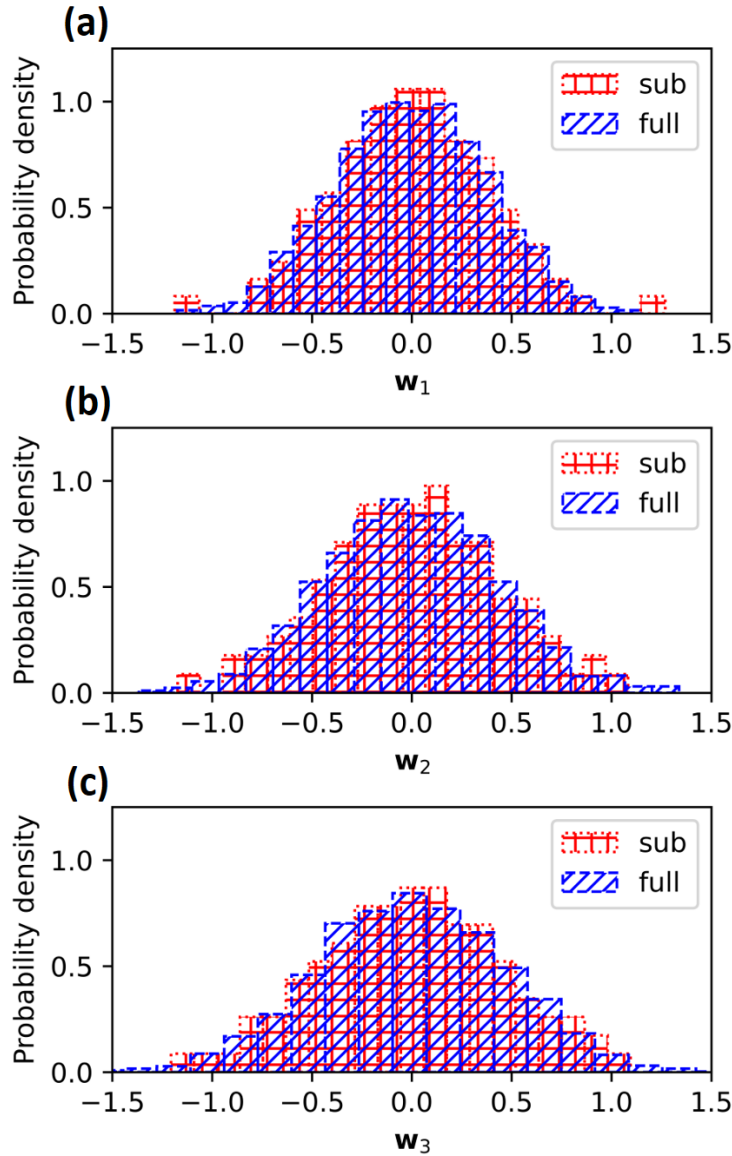
Figure 3-10: Histograms showing movement along each of the three subspace directions $\mathbf{w}_1$, $\mathbf{w}_2$, and $\mathbf{w}_3$ in **(a)**, **(b)**, and **(c)**, respectively. Blue bins show full kinetic uncertainty samples projected into the subspace directions, while red bins show samples directly taken from the subspace using uncertainty ranges projected from the literature-informed values of Eq. 2.1. The tighter distribution in $\mathbf{w}_1$ and wider distribution in $\mathbf{w}_3$ align in both sets of bins, indicating correct implementation.

With these subspace-informed samples, it was found that with computational savings of multiple orders of magnitude it is possible to reconstruct the full uncertainty profiles with strong accuracy. In Fig. 3-11a-b, the three sigma temperature uncertainty ranges of the centerline profile and near-nozzle profile are compared when using

55

just seven subspace-informed Latin Hypercube samples [75] against those with the full 2,000 samples, and accuracies of 70.4% and 82.3% were observed, respectively. The discrepancy in accuracy between these locations can be traced back to the results of Figs. 3-5 and 3-8 where general trends indicated stronger subspace performance in the high-strain flamelets and in the axial maximum temperature, and weaker subspace performance in the lower-strain flamelets and in the centerline maximum temperature.
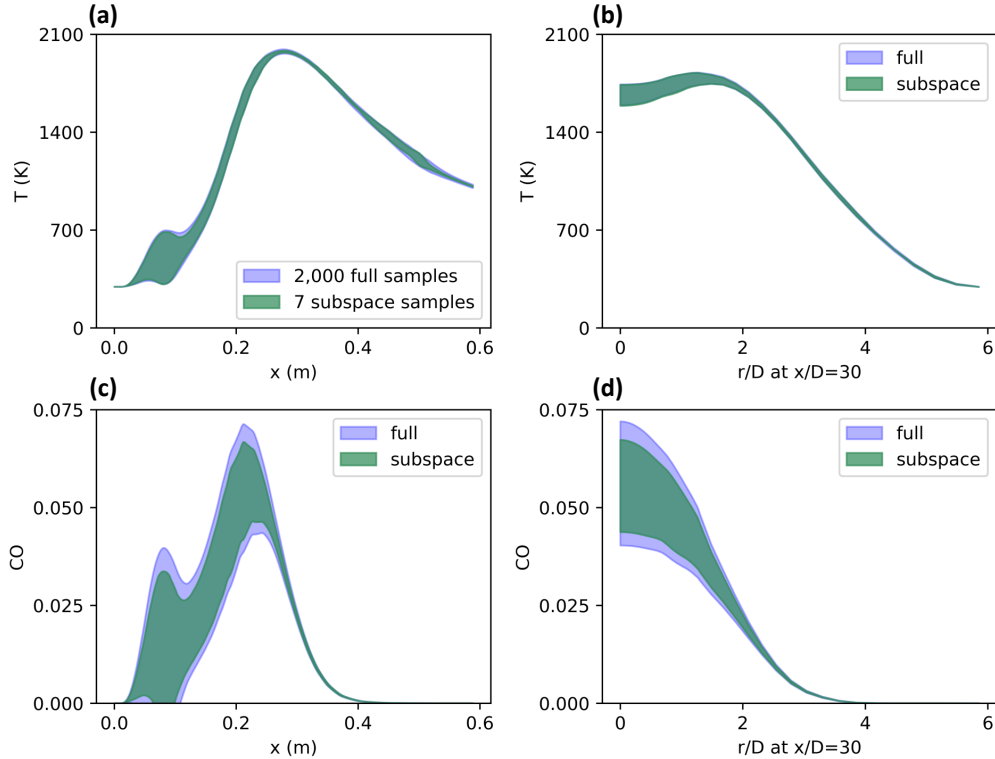

Figure 3-11: Uncertainty ranges for temperature and CO mass fractions at representative slices in the 2-D domain. The estimated ground truths are from 2,000 samples in the full kinetic uncertainty space. The subspace results are computed using just seven samples in the three-dimensional subspace. (a) Temperature uncertainty along the centerline. (b) Temperature uncertainty across the $x/D = 30$ near-nozzle slice. (c) CO mass fraction uncertainty along the centerline. (d) CO mass fraction uncertainty across the $x/D = 30$ near-nozzle slice.

The CO mass fraction uncertainty ranges are additionally plotted in Fig. 3-11c-d based on both the full 2,000-sample run as well as the subspace-reduced 7-sample run. The accuracies here were found to be 68.7% and 69.7%, respectively, for the centerline profile and near-nozzle profile. CO was not tracked in the surrogate

modelling and subspace reduction process, however, thus all agreement here is due to the strong coupling between the temperature profile and species evolution profiles. If higher-accuracy species uncertainty profiles are desired, users can either (1) replace the temperature prediction network with a species prediction network and otherwise retain an identical methodology for a subspace that is tailored to a single species profile, or (2) increase the size of the network output layer to facilitate the learning of temperature and/or multiple species profiles, and simply add the additional species-based local kinetic subspaces into the $\mathbf{A}$ matrix as was done in this work for the strain-dependent temperature profiles. Such generalizations are not considered here, and instead extrapolation capabilities of the temperature subspace to the CO species profiles are presented to highlight promise for such future applications.

Due to the relatively inexpensive turbulence model used in this work, it was possible to repeat this subspace-informed forward uncertainty propagation multiple times to confirm the reliability of this result. Between 7 and 50 subspace-informed perturbations were independently sampled for each trial. In Fig. 3-12, the accuracies of the uncertainty ranges of each of these runs are compared against the full-space 2,000 sample case. Greater than 70% and greater than 80% accuracy for the centerline and near-nozzle temperature uncertainty ranges, respectively, are observable at all sample numbers. In the samples leading up to 20, there is a noisy yet overall substantial trend of increasing accuracy. Past 20, the accuracy values tend to fairly stable quantities in the $80 - 90\%+$ range for temperatures and the $85 - 95\%+$ range for CO mass fractions. There is one noticeable outlier in the axial near-nozzle temperature agreement in the 40 sample case, which despite this still achieves 82.6% and 83.9% accuracy in the near-nozzle and centerline profiles, respectively. General trends indicate a continuation of the pattern of near-nozzle slices performing better than centerline slices, which is again unsurprising given the trends of Figs. 3-5 and 3-8. This discrepancy in accuracy combined with the stronger relative performance of subspace directions $\mathbf{w}_4$ through $\mathbf{w}_6$ in predicting the centerline maximum temperatures (as shown in Fig. 3-9) perhaps suggests that a five-dimensional subspace might substantially improve the centerline temperature uncertainty ranges thanks to the

noticeable trend of Fig. 3-9f, while the axial predictions would not improve as much. Regardless of these details, the uncertainty reductions shown here represent a large amount of computational savings in all cases. When compared against the greater than 2,000 samples needed to fully converge the uncertainty of the full kinetic space, the current subspace enables 300x fewer runs to achieve strong accuracy using just 7 samples. For cheaper simulations where the user is able to sample the subspace 30-50 times, the uncertainty ranges appear to converge with upwards of $80 - 90\%$ accuracy, depending on the sampling location. Large computational savings are similarly to be expected when compared against comparable or even larger chemical models than methane.
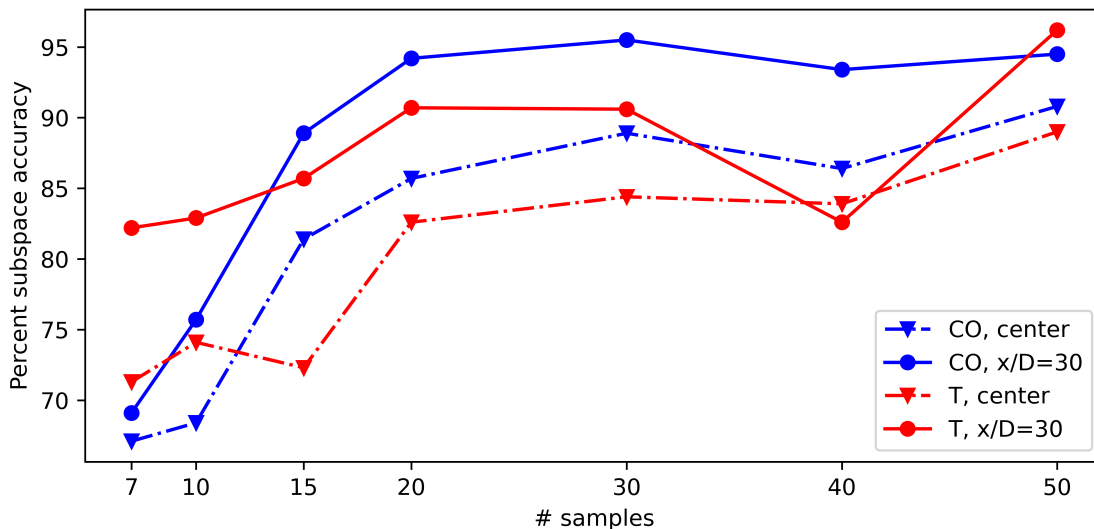

Figure 3-12: Percent accuracy of small-sample subspace uncertainty ranges against the set of 2,000 full model runs, calculated across various slices in the turbulent simulation domain. Temperature profile accuracies follow the pattern discussed in Fig. 3-8 of stronger performance closer to the nozzle. CO profiles were not included in the set of subspace targets but see fairly strong agreement nonetheless. The accuracy was strong in all cases, indicating that with as low as seven samples the reduced three-dimensional subspace provides useful uncertainty ranges, and that with upwards of 20 these uncertainty ranges become remarkably accurate.

For visualization of the case that is most likely to represent the converged uncertainty quantification result of the three-dimensional subspace, Fig. 3-13 is additionally provided. The plots in this figure contain the same information as Fig.

3-11, though using statistics from the run of 50 subspace-informed latin hypercube samples. As follows from Fig. 3-12, the agreement here is excellent overall, and represents a convincing improvement over the already strong results of Fig. 3-11. The selection of number of samples used in the final forward uncertainty propgation is thus another opportunity for users to tailor the method to their specific needs, with options available for good accuracy and extremely reduced computational cost, or low computational cost and remarkably high accuracy.
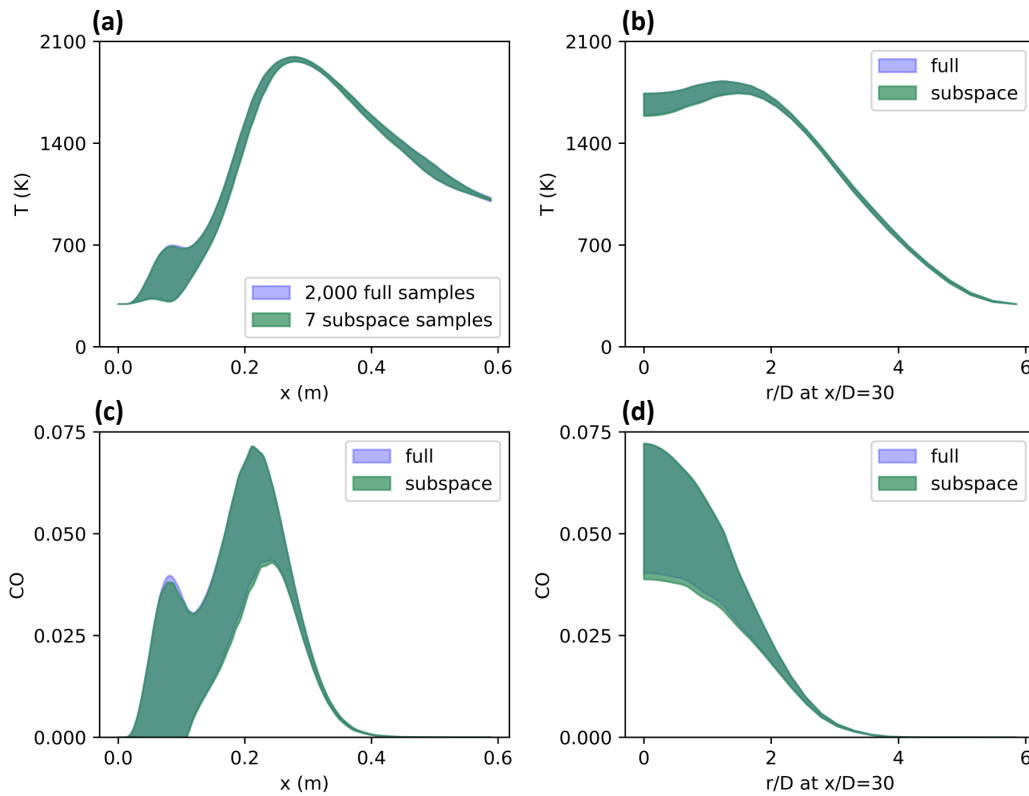

Figure 3-13: Uncertainty ranges for temperature and CO mass fractions at representative slices in the 2-D domain. The estimated ground truths are from 2,000 samples in the full kinetic uncertainty space. The subspace results are computed using just fifty samples in the three-dimensional subspace. **(a)** Temperature uncertainty along the centerline. **(b)** Temperature uncertainty across the $x/D = 30$ near-nozzle slice. **(c)** CO mass fraction uncertainty along the centerline. **(d)** CO mass fraction uncertainty across the $x/D = 30$ near-nozzle slice.

In addition to the cost savings when compared to full-scale forward uncertainty propagation, a more nuanced analysis of the computational savings can be made

around the sensitivity analysis results of Fig. 3-4. There, the benefit of the active subspace method in terms of more compact dimensional representations of the key kinetic parameters was discussed. The sensitivity analysis revealed more than ten highly sensitive reactions, individual perturbations of which would not even be possible with the seven samples used as a low-end benchmark here. Thus, even in the more realistic case where the computational savings of the current method are compared against a reduced mechanism or perturbations of highly sensitive reactions only (as opposed to the fully detailed mechanism), the proposed framework still offers a cheaper and more substantially reduced space within which users must sample. The proposed framework appears to require no fewer samples than [16] in order to characterize the same Sandia Flame D temperature uncertainties, indicating no increase in savings compared to that work (and perhaps even a decrease in savings if using a more conservative number of samples, such as 20 or 50). Due to the computational cost of the forward problem in [16], however, the ground truth was not reported there. Without this information, it is impossible to evaluate the accuracy of the ranges presented in [16], making detailed comparison of accuracy between these methods impossible. Apart from accuracy comparisons, the differing reduction methodology performed here allows for a handful of key performance metrics and analyses that are not possible with the methodology of [16]. Firstly, it enables accuracy estimation in the flamelet table, which based on Figs. 3-5 and 3-12 is seen to be a good indicator of the subspace's global accuracy in the larger turbulent simulation, especially in the more realistic case where 2,000 samples are not available for direct comparison. Next, the preceding discussion in this subsection also shows how the global subspace's accuracy metrics across the flamelet table can predict the spatial dependence of accuracy in the turbulent simulation, enabling local accuracy predictions in the turbulent case based on flow regime comparison against the cheap surrogate samples. Finally, this methodology allows for the direct relation of uncertainty responses to kinetic parameters, as was shown in Fig. 3-4. This tradeoff between computational cost, accuracy predictions, and kinetic interpretability is a decision that can be made based on the needs of the case at hand, though the turbulent simulation shown here highlights the

promise of this novel methodology in handling all three.

Chapter 4

Conclusions and Future Work

4.1 Conclusions

In this work, a complete framework for flamelet-based kinetic sensitivity reduction
in a two-dimensional turbulent combustion simulation was demonstrated. Using a
multi-target, neural network-accelerated active subspace reduction in the flamelet ta-
ble, a three-dimensional kinetic subspace was discovered that was able to reconstruct
the full temperature uncertainty profile of the Sandia Flame D with strong accuracy.
The accuracy of this reconstruction corresponded fairly well both globally and lo-
cally to the accuracy observed in the much cheaper flamelet simulations, allowing for
meaningful a priori error estimates across the turbulent flame profile even in the real-
istic case where expensive convergence testing cannot be carried out in the full-scale
turbulent simulation.

In addition to the strong uncertainty quantification results, the behavior of the
subspaces across both the flamelet table input parameters and the turbulent sim-
ulation spatial domain revealed notable insights into the shifting kinetic sensitivity
directions across these various input domains, which would not be possible to capture
using a standard, scalar quantity of interest sensitivity method. While the kinetic sen-
sitivities are more complex and strain rate-dependent than expected in the literature,
the multi-target methodology proposed here is robust and maintained high accuracy
and significant dimension reduction. The temperature-based subspace is also shown

to have good species profile predictive capabilities, with stronger species uncertainty results expected when the network and subspace portions of the methodology are adjusted to include species targets.

4.2   Future Work

The flexibility, multi-target applicability, predictable error ranges, low computational cost, and kinetic interpretability of this method make it a promising tool for efficient uncertainty quantification in similar small-scale turbulent combustion simulations as well as in more expensive large eddy simulations in the flamelet regime. In short, offloading the kinetic reduction cost to the cheap laminar flamelets allows for a reduction procedure that is entirely decoupled from and does not scale with the cost of a given turbulent combustion simulation, yet can still predict its uncertainty behavior well and with good a priori estimates of accuracy. These advantages open the door to a broad range of future research questions.

Only the Sandia Flame D was investigated in this work as a turbulent simulation in which to apply the novel methodology, but other flames at higher or lower Reynolds numbers or with different fuels or geometries may prove interesting as additional testing cases. The use of a flamelet-based approach is required due to the physics-informed kinetic argument, yet the Reynolds-averaged turbulence model used here represents a simple approach to treatment of the turbulence present in the flame. Thanks to the extremely efficient dimensional compression, future application in large eddy simulations is feasible and may provide insightful results. The flamelet table investigated here was additionally defined by the two-dimensional mixture fraction and strain rate phase space, though in certain unsteady or variable pressure cases higher-dimensional flamelet tables may be required. The use of an artificial neural network and the two-stage subspace reduction process were designed to enable efficient generalization, though such larger flamelet tables were not explicitly tested in this work. The two-stage subspace reduction process here also assumed uniformly one-dimensional subspaces across the phase space of the flamelet table, which was

based solely on heuristic testing and in this case performed very well. Additional optimization and treatment of these locally higher-dimension subspaces may further enhance results, especially as larger input spaces and more complex mechanisms are investigated.

Appendix A

Additional Tables

Table A.1: Coordinates of the five labelled points in Fig. B-1.

Label	a (1/s)	Z
1 ●	58.7	0.6
2 ●	5.33	0.55
3 ●	1.54	0.33
4 ●	136	0.22
5 ●	0.871	0.15

Table A.2: Index-ordered list of all unique reactions (18 total) present in the top 6 sensitivity indices of the five sampling locations of Fig. B-1. Little overlap in highly sensitive reactions across these five directions indicates strain and mixture fraction dependence of not only the kinetic sensitivity directions, as could be inferred from Fig. 3-6b, but also the highly sensitive kinetic indices, further demonstrating the efficient compression enabled by the active subspace methodology.

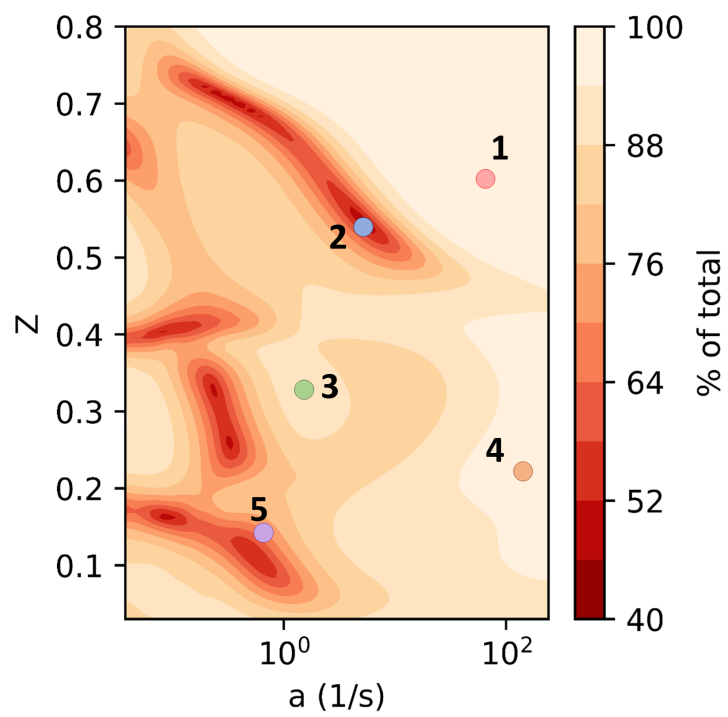| Index	Included Subspaces	Reaction
10	🔵	O + CH3 [=] H + CH2O
35	🔵 🟢 🟠	H + O2 + H2O [=] HO2 + H2O
37	🔴 🔵 🟢 🟠 🟣	H + O2 [=] O + OH
42	🟢	H + OH + M [=] H2O + M
47	🟣	H + H2O2 [=] OH + H2O
51	🔴 🟠 🟣	H + CH3 (+ M) [=] CH4 (+ M)
52	🔴 🔵	H + CH4 [=] CH3 + H2
54	🟣	H + HCO [=] H2 + CO
78	🔵	H + HCCO [=] CH2(S) + CO
84	🟢	2 OH (+ M) [=] H2O2 (+ M)
97	🔴	OH + CH4 [=] CH3 + H2O
98	🟢 🟠 🟣	OH + CO [=] H + CO2
103	🟣	OH + CH3OH [=] CH2OH + H2O
118	🟠	HO2 + CH3 [=] OH + CH3O
130	🔵	CH + CO (+ M) [=] HCCO (+ M)
156	🔴 🟢	2 CH3 (+ M) [=] C2H6 (+ M)
186	🔴	C2H3 + O2 [=] O + CH2CHO
210	🟠	CH3 + C2H4 (+ M) [=] C3H7 (+ M)

Appendix B

Additional Figures

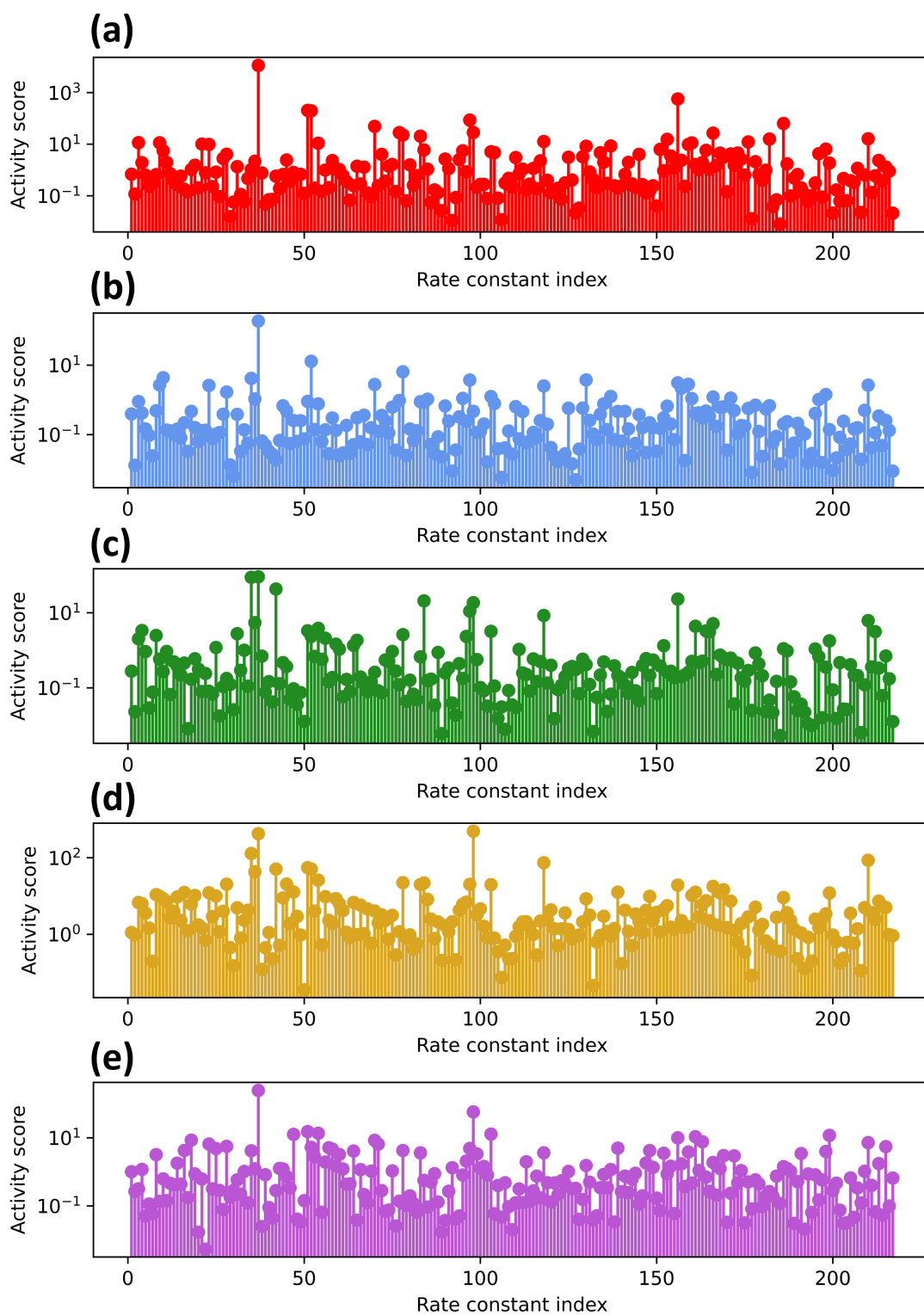Figure B-1: Copy of Fig. 3-6a, with five points labelled.

Figure B-2: Activity scores of the (a, Z)-local subspaces at the locations specified in Fig. B-1 and Table A.1 in **(a-e)**, respectively.

Bibliography

[1] Frank Ham, Sourabh Apte, Gianluca Iaccarino, Xiao-Hua Wu, Marcus Herrmann, George Constantinescu, Krishnan Mahesh, and Parviz Moin. Unstructured LES of Reacting Multiphase Flows in Realistic Gas Turbine Combustors, January 2003. NTRS Author Affiliations: Stanford Univ., Iowa Univ., Minnesota Univ. NTRS Document ID: 20040031696 NTRS Research Center: Headquarters (HQ).

[2] Stefan Buhl, Felix Dietzsch, Claudia Buhl, and Christian Hasse. Comparative study of turbulence models for scale-resolving simulations of internal combustion engine flows. *Computers & Fluids*, 156:66–80, October 2017.

[3] ZhenXun Gao and ChunHian Lee. A numerical study of turbulent combustion characteristics in a combustion chamber of a scramjet engine. *Science China Technological Sciences*, 53(8):2111–2121, August 2010.

[4] Jianan Zhang, Valerie L. Muldoon, and Sili Deng. Accelerated synthesis of Li(Ni0.8Co0.1Mn0.1)O2 cathode materials using flame-assisted spray pyrolysis and additives. *Journal of Power Sources*, 528:231244, April 2022.

[5] Xing Yuan, Menglei Qing, Lingquan Meng, and Haibo Zhao. One-Step Synthesis of Nanostructured Cu–Mn/TiO2 via Flame Spray Pyrolysis: Application to Catalytic Combustion of CO and CH4. *Energy & Fuels*, 34(11):14447–14457, November 2020. Publisher: American Chemical Society.

[6] Ping Ping, QingSong Wang, PeiFeng Huang, Ke Li, JinHua Sun, DePeng Kong, and ChunHua Chen. Study of the fire behavior of high-energy lithium-ion batteries with full-scale burning test. *Journal of Power Sources*, 285:80–89, July 2015.

[7] Dhananjay Mishra, Peng Zhao, and Ankur Jain. Thermal Runaway Propagation in Li-ion Battery Packs Due to Combustion of Vent Gases. *Journal of The Electrochemical Society*, 169(10):100520, October 2022. Publisher: IOP Publishing.

[8] Christophe Duwig, Karl-Johan Nogenmyr, Ck Chan, and Matthew Dunn. Large Eddy Simulations of a piloted lean premix jet flame using finite-rate chemistry. *Combustion Theory and Modelling*, 15:537–568, August 2011.

[9] Tianfeng Lu and Chung K. Law. Toward accommodating realistic fuel chemistry in large-scale computations. *Progress in Energy and Combustion Science*, 35(2):192–215, 2009.

[10] Assaad R. Masri. Challenges for turbulent combustion. *Proceedings of the Combustion Institute*, 38(1):121–155, January 2021.

[11] Thomas M. Gruenberger, Mohammad Moghiman, Philip J. Bowen, and Nick Syred. Dynamics of soot formation by turbulent combustion and thermal decomposition of natural gas. *Combustion Science and Technology*, 174(5-6):67–86, May 2002. Publisher: Taylor & Francis _eprint: https://doi.org/10.1080/713713038.

[12] Hernando Maldonado Colmán, Nasser Darabiha, Denis Veynante, and Benoît Fiorina. A turbulent combustion model for soot formation at the LES subgrid-scale using virtual chemistry approach. *Combustion and Flame*, 247:112496, January 2023.

[13] Pascale Domingo and Luc Vervisch. Recent developments in DNS of turbulent combustion. *Proceedings of the Combustion Institute*, 2022.

[14] Jacqueline H. Chen, Alok Choudhary, Bronis de Supinski, M. DeVries, Evatt R. Hawkes, Scott Klasky, Wei-Keng Liao, K. L. Ma, John Mellor-Crummey, Norbert Podhorszki, Ramanan Sankaran, Sameer Shende, and Chun Sang Yoo. Terascale direct numerical simulations of turbulent combustion using S3D. *Computational Science & Discovery*, 2(1):015001, January 2009.

[15] Fan Zhang, Rixin Yu, and Xue Song Bai. Direct numerical simulation of PRF70/air partially premixed combustion under IC engine conditions. *Proceedings of the Combustion Institute*, 35(3):2975–2982, January 2015.

[16] Michael E. Mueller, Gianluca Iaccarino, and Heinz Pitsch. Chemical kinetic uncertainty quantification for Large Eddy Simulation of turbulent nonpremixed combustion. *Proc. Combust. Inst.*, 34(1):1299–1306, 2013.

[17] Yihao Tang and Venkat Raman. Large eddy simulation of premixed turbulent combustion using a non-adiabatic, strain-sensitive flamelet approach. *Combustion and Flame*, 234:111655, December 2021.

[18] Kerry S. Klemmer and Michael E. Mueller. Hierarchical model form uncertainty quantification for turbulent combustion modeling. *Combustion and Flame*, 221:288–295, November 2020.

[19] Michael E. Mueller and Venkat Raman. Model form uncertainty quantification in turbulent combustion simulations: Peer models. *Combust. Flame*, 187:137–146, 2018.

[20] Mohammad Khalil, Guilhem Lacaze, Joseph C. Oefelein, and Habib N. Najm. Uncertainty quantification in LES of a turbulent bluff-body stabilized flame. *Proceedings of the Combustion Institute*, 35(2):1147–1156, January 2015.

[21] Xiaoxu Zhang, Nana Wang, Qing Xie, Hua Zhou, and Zhuyin Ren. Global sensitivity analysis and uncertainty quantification of soot formation in an n-dodecane spray flame. *Fuel*, 320:123855, 2022.

[22] Weiqi Ji, Zhuyin Ren, Youssef Marzouk, and Chung K. Law. Quantifying kinetic uncertainty in turbulent combustion simulations using active subspaces. *Proc. Combust. Inst.*, 37(2):2175–2182, 2019.

[23] Jan Mateu Armengol, Olivier Le Maître, and Ronan Vicquelin. Bayesian calibration of a methane-air global scheme and uncertainty propagation to flame-vortex interactions. *Combust. Flame*, 234:111642, December 2021.

[24] Rodger E. Cornell, Mark C. Barbet, Joe Lee, and Michael P. Burke. NH3 oxidation by NO2 in a jet-stirred reactor: The effect of significant uncertainties in H2NO kinetics. *Applications in Energy and Combustion Science*, 12:100095, 2022.

[25] Michael P. Burke. Harnessing the Combined Power of Theoretical and Experimental Data through Multiscale Informatics. *International Journal of Chemical Kinetics*, 48(4):212–235, 2016.

[26] James A. Miller, Raghu Sivaramakrishnan, Yujie Tao, C. Franklin Goldsmith, Michael P. Burke, Ahren W. Jasper, Nils Hansen, Nicole J. Labbe, Peter Glarborg, and Judit Zádor. Combustion chemistry in the twenty-first century: Developing theory-informed chemical kinetics models. *Progress in Energy and Combustion Science*, 83:100886, 2021.

[27] Hai Wang and David A. Sheen. Combustion kinetic model uncertainty quantification, propagation and minimization. *Progress in Energy and Combustion Science*, 47:1–31, 2015.

[28] Bin Yang. Towards predictive combustion kinetic models: Progress in model analysis and informative experiments. *Proc. Combust. Inst.*, 38(1):199–222, 2021.

[29] Weiqi Ji, Jiaxing Wang, Olivier Zahm, Youssef Marzouk, Bin Yang, Zhuyin Ren, and Chung Law. Shared Low-Dimensional Subspaces for Propagating Kinetic Uncertainty to Multiple Outputs. *Combust. Flame*, 190:146–157, 2018.

[30] Katerina Konakli and Bruno Sudret. Polynomial meta-models with canonical low-rank approximations: Numerical insights and comparison to sparse polynomial chaos expansions. *Journal of Computational Physics*, 321:1144–1169, 2016.

[31] Yue Zhang, Wendi Dong, Laurien A. Vandewalle, Rui Xu, Gregory P. Smith, and Hai Wang. Neural network approach to response surface development for

reaction model optimization and uncertainty minimization. *Combust. Flame*, 251:112679, 2023.

[32] Thierry Crestaux, Olivier Le Maı̂tre, and Jean-Marc Martinez. Polynomial chaos expansion for sensitivity analysis. *Reliability Engineering & System Safety*, 94(7):1161–1172, July 2009.

[33] Michael Frenklach, Hai Wang, and Martin J. Rabinowitz. Optimization and analysis of large chemical kinetic mechanisms using the solution mapping method—combustion of methane. *Progress in Energy and Combustion Science*, 18(1):47–73, 1992.

[34] Gaetano Esposito, Brendyn G. Sarnacki, and Harsha K. Chelliah. Uncertainty propagation of chemical kinetics parameters and binary diffusion coefficients in predicting extinction limits of hydrogen/oxygen/nitrogen non-premixed flames. *Combustion Theory and Modelling*, 16:1029–1052, 2012.

[35] Matthew T. Reagan, Habib N. Najm, Philippe P. Pébay, Omar M. Knio, and Roger G. Ghanem. Quantifying uncertainty in chemical systems modeling. *International Journal of Chemical Kinetics*, 37(6):368–382, 2005.

[36] Judit Zádor, István Gy. Zsély, Tamás Turányi, Marco Ratto, Stefano Tarantola, and Andrea Saltelli. Local and Global Uncertainty Analyses of a Methane Flame Model. *The Journal of Physical Chemistry A*, 109(43):9795–9807, 2005.

[37] Shuang Li, Bin Yang, and Fei Qi. Accelerate global sensitivity analysis using artificial neural network algorithm: Case studies for combustion kinetic model. *Combust. Flame*, 168:53–64, 2016.

[38] Paul G. Constantine and Paul Diaz. Global sensitivity metrics from active subspaces. *Reliability Engineering & System Safety*, 162:1–13, 2017.

[39] Yujie Tao and Hai Wang. Joint probability distribution of Arrhenius parameters in reaction model optimization and uncertainty minimization. *Proc. Combust. Inst.*, 37(1):817–824, 2019.

[40] David A. Sheen and Hai Wang. The method of uncertainty quantification and minimization using polynomial chaos expansions. *Combust. Flame*, 158(12):2358–2374, 2011.

[41] Norbert Peters. Laminar diffusion flamelet models in non-premixed turbulent combustion. *Progress in Energy and Combustion Science*, 10(3):319–339, January 1984.

[42] Norbert Peters. *Turbulent Combustion*. Cambridge Monographs on Mechanics. Cambridge University Press, Cambridge, 2000.

[43] Nana Wang, Qing Xie, Xingyu Su, and Zhuyin Ren. Quantification of modeling uncertainties in turbulent flames through successive dimension reduction. *Combust. Flame*, 222:476–489, 2020.

[44] Paul G. Constantine, Eric Dow, and Qiqi Wang. Active Subspace Methods in Theory and Practice: Applications to Kriging Surfaces. *SIAM Journal on Scientific Computing*, 36(4):A1500–A1524, 2014.

[45] James C. Sutherland and Alessandro Parente. Combustion modeling using principal component analysis. *Proc. Combust. Inst.*, 32(1):1563–1570, 2009.

[46] Sandor Vajda, Peter Valko, and Tamás Turányi. Principal component analysis of kinetic models. *International Journal of Chemical Kinetics*, 17(1):55–81, 1985.

[47] Paul Constantine and David Gleich. Computing active subspaces with Monte Carlo, 2015. arXiv:1408.0545 [math].

[48] Paul G. Constantine. *Active Subspaces*. SIAM Spotlights. Society for Industrial and Applied Mathematics, 2015.

[49] Manav Vohra, Alen Alexanderian, Hayley Guy, and Sankaran Mahadevan. Active subspace-based dimension reduction for chemical kinetics applications with epistemic uncertainty. *Combust. Flame*, 204:152–161, 2019.

[50] Paul G. Constantine, Michael Emory, Johan Larsson, and Gianluca Iaccarino. Exploiting active subspaces to quantify uncertainty in the numerical simulation of the HyShot II scramjet. *Journal of Computational Physics*, 302:1–20, 2015.

[51] Benjamin C. Koenig, Weiqi Ji, and Sili Deng. Kinetic subspace investigation using neural network for uncertainty quantification in nonpremixed flamelets. *Proc. Combust. Inst.*, 2022.

[52] David G. Goodwin, Raymond L. Speth, Harry K. Moffat, and Bryan W. Weber. Cantera: An object-oriented software toolkit for chemical kinetics, thermodynamics, and transport processes. `https://www.cantera.org`, 2021. Version 2.5.1.

[53] Gregory P. Smith, David M. Golden, Michael Frenklach, Nigel W. Moriarty, Boris Eiteneer, Mikhail Goldenberg, C. Thomas Bowman, Ronald K. Hanson, Soonho Song, William C. Gardiner, Jr., Vitali V. Lissianski, and Zhiwei Qin. Gri-mech 3.0. `http://combustion.berkeley.edu/gri-mech/`.

[54] David A. Sheen, Xiaoqing You, Hai Wang, and Terese Løvås. Spectral uncertainty quantification, propagation and optimization of a detailed kinetic model for ethylene combustion. *Proc. Combust. Inst.*, 32(1):535–542, 2009.

[55] James Duvall, Karthik Duraisamy, and Shaowu Pan. Non-linear Independent Dual System (NIDS) for Discretization-independent Surrogate Modeling over Complex Geometries. *arXiv:2109.07018 [physics]*, 2021.

[56] Lu Lu, Pengzhan Jin, Guofei Pang, Zhongqiang Zhang, and George Em Karniadakis. Learning nonlinear operators via DeepONet based on the universal approximation theorem of operators. *Nature Machine Intelligence*, 3(3):218–229, 2021.

[57] Jiaxing Wang, Zijun Zhou, Keli Lin, Chung K. Law, and Bin Yang. Facilitating Bayesian analysis of combustion kinetic models with artificial neural network. *Combust. Flame*, 213:87–97, 2020.

[58] David E. Rumelhart, Geoffrey E. Hinton, and Ronald J. Williams. Learning representations by back-propagating errors. *Nature*, 323(6088):533–536, 1986.

[59] Kevin M. Gitushi, Rishikesh Ranade, and Tarek Echekki. Investigation of deep learning methods for efficient high-fidelity simulations in turbulent combustion. *Combust. Flame*, 236:111814, 2022.

[60] Huaibo Chen, Weiqi Ji, Séan J. Cassady, Alison M. Ferris, Ronald K. Hanson, and Sili Deng. Using shock tube species time-histories in Bayesian parameter estimation: Effective independent-data number and target selection. *Proc. Combust. Inst.*, 2022.

[61] Richard Liaw, Eric Liang, Robert Nishihara, Philipp Moritz, Joseph E. Gonzalez, and Ion Stoica. Tune: A Research Platform for Distributed Model Selection and Training. *arXiv:1807.05118 [cs, stat]*, 2018.

[62] Kaiming He, Xiangyu Zhang, Shaoqing Ren, and Jian Sun. Deep Residual Learning for Image Recognition. In *2016 IEEE Conference on Computer Vision and Pattern Recognition (CVPR)*, pages 770–778, 2016.

[63] Stefan Elfwing, Eiji Uchibe, and Kenji Doya. Sigmoid-Weighted Linear Units for Neural Network Function Approximation in Reinforcement Learning. *arXiv:1702.03118 [cs]*, 2017.

[64] Diederik P. Kingma and Jimmy Ba. Adam: A Method for Stochastic Optimization. *arXiv:1412.6980 [cs]*, 2017.

[65] Thomas Fiala and Thomas Sattelmayer. Nonpremixed Counterflow Flames: Scaling Rules for Batch Simulations. *Journal of Combustion*, 2014:484372, 2014.

[66] Robert S. Barlow and Jonathan H. Frank. Effects of turbulence on species mass fractions in methane/air jet flames. *Symp. (Int.) Combust.*, 27(1):1087–1095, 1998.

[67] Robert S. Barlow and Jonathan H. Frank. Piloted CH4/Air Flames C, D, E, and F – Release 2.1. `https://tnfworkshop.org/data-archives/`, 2007.

[68] H.A.J.A van Kuijk, Rob J. M. Bastiaans, Jeroen A. van Oijen, and Laurentius P.H. de Goey. Modelling NOx-formation for application in a biomass combustion furnace. In *Proceedings of the European Combustion Meeting*, 2005.

[69] Haifeng Wang and Yiliang Chen. Steady flamelet modelling of a turbulent non-premixed flame considering scalar dissipation rate fluctuations. *Fluid Dynamics Research*, 37(3):133, 2005.

[70] Claudia Pfeiler and Harald Raupenstrauch. Application of Different Turbulence Models to Study the Effect of Local Anisotropy for a Non-Premixed Piloted Methane Flame. *Comput. Aided Chem. Eng.*, 28:49–54, 2010.

[71] Tsan-Hsing Shih, William W. Liou, Aamir Shabbir, Zhigang Yang, and Jiang Zhu. A new k-epsilon eddy viscosity model for high reynolds number turbulent flows. *Computers & Fluids*, 24(3):227–238, 1995.

[72] *ANSYS Fluent Theory Guide, Release 15.0, ANSYS, Inc. (2013)*.

[73] Weiqi Ji, Tianwei Yang, Zhuyin Ren, and Sili Deng. Dependence of kinetic sensitivity direction in premixed flames. *Combust. Flame*, 220:16–22, 2020.

[74] Adonios N. Karpetis and Robert S. Barlow. Measurements of scalar dissipation in a turbulent piloted methane/air jet flame. *Proc. Combust. Inst.*, 29(2):1929–1936, 2002.

[75] Michael D. McKay, Richard J. Beckman, and William J. Conover. Comparison of Three Methods for Selecting Values of Input Variables in the Analysis of Output from a Computer Code. *Technometrics*, 21(2):239–245, 1979.